Long-term effects of X-ray irradiation on genome and metabolism of mammalian cells

(X 線照射が哺乳類細胞の遺伝子および代謝に及ぼす長期影響)

Eri Hirose

A thesis submitted to the Graduate School of Science and Engineering,
Ibaraki University, for consideration for the degree of

DOCTOR OF PHILOSOPHY

March 2023

ACKNOWLEDGEMENTS

The work presented in this thesis would not have been possible without the loving care of many people. I would like to give my best thanks to my supervisor, Dr. Akinari Yokoya of the National Institutes for Quantum Science and Technology (QST), for his continuous guidance in my studies. Many of things he gave me would drive me to do great work. He is a mentor of my life, and everything I have achieved to date is because of him. I cannot thank him enough for all the help and time he took out to guide me upon my studies. I would also like to thank Dr. Keiji Suzuki of Nagasaki University for his suggestions and sound advice in all the time of research. He always gives me kind words to encourage me. His attitude of tackling work had a profound influence on me. It is incredible experience to work with him whose skills and talents are remarkable.

I must express my gratitude to Dr. Miho Noguchi of QST for her kind support and advice on experimental design. Without her encouragement, it would not have been possible to materialize this thesis. I would like to thank Dr. Hisanori Fukunaga for giving me the opportunity to be a part of his research on the effect of radiation treatment. These his continuous hard work and wish as a medical doctor to improve the quality of life of people give an enormous impact on me. I appreciate two Ph. D. students at Ibaraki University, Mr. Kai Nishikubo and Ms. Yui Obata, for their laboratory management.

Their dedication has kept me going to challenge further experiments. I would also like to thank Mr. Tomokazu Ihara and Mr. Tomoyuki Saito of Ibaraki University for their experimental support on treatment of mammalian cells and help in keeping me positive.

Finally, my appreciation goes out to all members of my family and friends for their supports all throughout the ups and downs of my research. Without their tremendous understanding and encouragement, it would be impossible to complete my study.

Eri Hirose
March 2023

DECLARATION

This dissertation is submitted for the degree of Doctor of Philosophy in accordance with the regulations of Ibaraki University. I hereby certify that the work contained herein is the result of my own original research and has not previously been submitted for the award of a degree at this or any other academic institution. Any material borrowed from outside sources has been properly cited where applicable.

PUBLICATIONS AND PRESENTATIONS

Publications:

1. Hirose, E.; Yokoya, A.; Kawamura, K.; Suzuki, K. Analysis of differentially expressed genes on human X chromosome harboring large deletion induced by X-rays. *J Radiat Res* **2023**, doi:10.1093/jrr/rrac093. Online ahead of print publication.

2. Hirose, E.; Noguchi, M.; Ihara, T.; Yokoya, A. Mitochondrial Metabolism in X-Irradiated Cells Undergoing Irreversible Cell-Cycle Arrest. *Int J Mol Sci* **2023**, 24(3):1833, doi:10.3390/ijms24031833.

3. Hirose, E.; Suzuki, K.; Yokoya, A. Molecular Configuration of Human Genome Neighboring Megabase-Sized Large Deletions Induced by X-Ray Irradiation. *Radiat Res* **2021**, *195*, 561-567, doi:10.1667/RR15229.1.

4. Fukunaga, H.; Kaminaga, K.; Hirose, E.; Watanabe, R.; Usami, N.; Prise, K.M.; Yokoya, A. No Intercellular Regulation of the Cell Cycle among Human Cervical Carcinoma HeLa Cells Expressing Fluorescent Ubiquitination-Based Cell-Cycle Indicators in Modulated Radiation Fields. *Int J Mol Sci* **2021**, 22(23):12785, doi:10.3390/ijms222312785.

Awarded presentation:

優秀演題発表賞 [Best Presentation Award]

Hirose E, Yokoya A, Suzuki K. Genome signature analysis of Megabase-sized large deletions induced by X-irradiation. The 63rd Annual Meeting of the Japanese Radiation Society (JRRS), October 15-17, 2020, Fukushima, Online (Oral presentation).

Presentations:

Hirose E, Yokoya A, Suzuki K. Analysis of DNA deletion patterns as radiation signature underlying genomic instability. The 64th Annual Meeting of the Japanese Radiation Society (JRRS), September 22-24, 2021, Mito, Online (Oral presentation).

Hirose E, Yokoya A, Suzuki K. 放射線誘発遺伝的不安定性の起源の探索 [Searching for the origin of radiation-induced genetic instability]. The 19th Remote Young Researchers and Engineers Meeting by North Kanto Branch of Atomic Energy Society of Japan (AESJ), October 28, 2020, Online (Oral presentation).

ABSTRACT

Various biologically delayed effects of ionizing radiation, involving radiation-induced carcinogenesis, are caused by the genetic alternations in radiation surviving cells. These phenomena are very slow processes with a timescale of hours or days, in other words “long-term effects”, when compared to the rapid molecular processes triggered by radiation, such as deoxyribonucleic acid (DNA) damage and its repair with short timescales of femto- to milli-seconds. Thus, there is a large gap between the prompt radiation processes and the delayed long-term effects. The progeny of radiation surviving cells are likely to have a survival rate similar to that of non-irradiated cells because the progeny cells is expected to completely repair the most lethal type of DNA damage, double strand breaks (DSBs). However, delayed mutations and cell death have been observed to be induced after the cells have undergone several cell-divisions. Radiation-induced irreversible cell-cycle arrested cells (i.e., senescence-like cells) may also cause the delayed mutations. The existence of these progeny cells in organs could affect the surrounding normal cells through certain secretions resulting from the specific metabolism to the progeny cells. Here, the long-term effects of ionizing radiation are studied with a unique method that discusses the effects from two perspectives: genomic and metabolic effects.

Genomic instability, one of the causes of carcinogenesis, has an impact on the genes flanking the radiation-induced large deletion, which could be transmitted to the progeny of radiation-surviving cells over many generations, even though the DNA repair process has already been completed in the parental cells. Simian virus40 (SV40)-immortalized normal human fibroblasts (parental cells as the control, GM638) and their three mutant clones, previously established as cell lines harboring a large deletion site at *hypoxanthine-phosphoribosyltransferase 1* (*HPRT1*) by exposure to X-rays as typical progeny of radiation surviving cell lines, were studied. First, real-time quantitative PCR (qPCR) with 31 general STS markers and 15 originally designed primers, was used to reveal the landscape neighboring the large deletion. The DNA deletions were distributed in the patchwork pattern in the specific regions between 130-137 mega base (Mb) positions, and they were partially similar but clearly different among the three mutant clones. The possible mechanism underlying the induction of the patchwork pattern is that non-DSB-type clustered DNA damage sites, such as base lesions, single strand breaks (SSBs), or apurinic/apyrimidinic sites (abasic sites or AP sites), are multiply produced by a single radiation track that induces ionization or excitation to both chromosomes and water. These clusters could be converted into subsequent DSBs by glycosylase/AP lyase activities of base excision repair (BER) proteins.

These findings suggest that the patchwork structure of DNA deletions is involved in the modifying gene expression on X chromosome. Therefore, gene expression regulation was examined using a DNA microarray and quantitative reverse transcription PCR (RT-qPCR) method to reveal radiation-induced gene regulation of the entire X chromosome in the three clones. The evidence showed that the effect on genes in the progeny cells was not limited to the genes flanking the deleted regions but was spread over the entire X chromosome. Most of the 12 genes tested showed similar expression trends of up- or down-regulation; however, some of the genes had different regulation levels among the mutant clone cells, and, furthermore, some genes showed contradictory expressions. The observed alterations of gene expression levels possibly due to chromosome rearrangement, and this would be associated with spatial gene organization, such as topologically associating domains (TADs). In the domains, two compartments, namely active A and inactive B compartment corresponding to open chromatin and closed chromatin, respectively, are thought to be exchanged each other during cell-cycle progression. This alteration in the domains could be an origin of the contradictory gene expressions among the progeny cells. They may have radiation-specific gene regulation that would be different from that of the normal cells. These findings provide a new aspect of gene expression patterns as “radiation signatures”.

The metabolic effect of radiation could be significant in cells with irreversibly arrested cell cycle. The permanent cellular states are induced by pro-aging stressors, including exposure to ionizing radiation. These cells were thought to be inactive in terms of energy metabolism as a consequence of the unnecessary consumption of energy for cell division. However, the obtained evidence overturns this prevailing orthodoxy. WI-38 human primary fibroblast cells and BJ-5ta human h-TERT-immortalized fibroblast cells were exposed to 20 Gy of X rays and cultured for up to 9 days after irradiation to induce irreversible cell-cycle arrest. Mitochondrial morphology and its membrane potential were examined in the cells using the mitochondrial-specific fluorescent reagents, MitoTracker Green (MTG) and 5,5′,6,6′-tetraethyl-benzimidazolylcarbocyanine iodide (JC-1), respectively. The fluorescence of the latter reagent changes specifically depending on the mitochondrial potential.

The ratio of the mean MTG-stained total mitochondrial area per unit cell area decreased successively for 9 days after X-ray irradiation. The fraction of high mitochondrial membrane potential area visualized by JC-1 staining reached its minimum at 2 days after irradiation, and then increased for up to 9 days (in particular, WI-38 cells increased 1.8-fold the value of the control). Their chronological changes indicate that the mitochondrial area in the irreversible cell-cycle arrested cells did not show an increase relative to their cellular area expansion. Alternatively, they became highly active 2 to 5 days after irradiation as revealed by JC-1 staining. The evidence suggests that the energy metabolism in the X-ray-induced irreversible cell-cycle arrested cells is highly activated compared to non-irradiated normal cells, even though they do not undergo cell division. This indicates that mitochondria in irreversibly cell-cycle arrested cells contribute to homeostasis by producing extra ATP for various senescence-specific contexts: senescent cell-specific heterochromatin structures (senescence-associated heterochromatic foci), activation of the p53-p21 and p16-Rb pathways to arrest the cell cycle, avoidance of mitosis and transition to the G1 phase, or the senescence-associated secretory phenotype (SASP). Their highly metabolic products can have an impact on the surrounding normal cells. These findings serve as a window into the understanding of the role of long-lived irradiated cells in normal organs.

In conclusion, studies of genomic and metabolic effects as cellular responses to ionizing radiation are essential to elucidate the mechanism of long-term effects of radiation in organs or the whole body. The processes of the progeny or long-lived cells are significantly involved in the secondary carcinogenesis induced by radiotherapy. The present study may also provide a step forward in accurately assessing the long-term health effects of atomic bomb survivors or residents near the Fukushima Daiichi nuclear power plant who may be faced with anxiety of radiation exposure resulting from the accident.

TABLE OF CONTENTS

LIST OF FIGURES AND TABLES

CHAPTER 1: Introduction

Figure 1-1 **Timescale of the action of ionizing radiation in mammalian cells.**

Various events in mammalian cells occur over a wide range of timescale. Direct and indirect effects of ionizing radiation can cause cell damage and resulting carcinogenesis.

CHAPTER 2: Genomic effects

Figure 2-1 **Microscopic images of GM638, 3X-40, 3X-41, and 3X-45 cells on a dish.**

The parental cells, GM638, and its clones of the progeny of radiation surviving cells, 3X-40, 3X-41, and 3X-45 are shown in the phase contrast microscopic images.

Figure 2-2 ***HPRT 1* mutation assay procedure.**

Cells were exposed to 3 Gy of X rays and then 60 µM of 6-TG was added to obtain 6-TG-resistant clones. After two weeks of incubation, the colony-formed progeny of radiation surviving cells were randomly selected and named as 3X-40, 3X-41, or 3X-45 (performed by Nagasaki University).

Table 2-2 **Locations and sequences of primers used for RT-qPCR analysis.**

Figure 2-6 **Thermal cycling profile for RT-qPCR analysis.**

The PCR reaction mixture was initially heated at 50 ºC for 2 min, followed by initial denaturation at 95 ºC for 30 s. The PCR cycling consisted of denaturation at 95ºC for 15 s and annealing/extension at 60 ºC for 30 s. The number of amplification cycles was set to be 35. The melting curve was then analyzed according to the following protocol: 95 ºC for 15 s, 60 ºC for 15 s, and 95 ºC for 15 s.

Figure 2-7 **Positive and negative results of qPCR analysis.**

One of the positive and negative results of amplification and melting curves are shown. Left: The horizontal axes represent the number of PCR cycles, and the vertical axes represent the fluorescence intensity. Right: The horizontal axes represent the temperature, and the vertical axes represent -ΔF/ΔT (fluorescence change/temperature change). The samples were divided into three wells of a 96-well plate, and the results are represented by three lines.

(A) Positive results obtained with the DXS7888 primer against 3X-40 clones are shown. Left: The mean value of Ct was 19.69. Right: A single peak was observed by melting curve analysis.

(B) The negative results obtained with the DXS7888 primer against 3X-41 clones are shown. Left: The mean value of Ct was 35.89. Right: The observed multiple peaks of the melting curves were not consistent among the three observations.

Table 2-3 ***MARA5*** **expression level in 3X-40 cells, calculated by the ΔΔCT method.**

Figure 2-8 **DNA deletion in a patchwork pattern.**

Results of qPCR using 21 STS primers and 15 newly designed primer pairs (named as Designated 1-15) against clones. Clone GM638 is the control (parent cells). Clones 3X-40, 3X-41, and 3X-45 are the progeny of radiation surviving cells with large DNA deletions. X0-1 and X0-2 are spontaneous mutant clones. 3X-2 and 3X-21 are 3 Gy X-ray induced point mutant clones. The entire *HPRT1* exon is present in all cell types. The genomic region located on the X chromosome from 130 to 137 Mb was examined. Positive and negative PCR results are shown as blue and red dots, respectively. The *HPRT1* locus is shown as an orange box. The enlarged figures of region 1 and region 2 are shown at the bottom of the main figure.

Figure 2-11 **RT-qPCR analysis for the twelve genes selected from the microarray analysis.**

One gene per peak in Figure 2-10 was randomly selected for RT-qPCR analysis. All data were normalized to the reference gene, *ACTB (actin beta)*, and expressed as relative to the control, GM638 cells. Gene symbols (locations and sequences of primers are shown in Table 2-2) on the horizontal axis are arranged in the order of gene location from upstream (left) to downstream (right) of the X chromosome. The fold change of gene expression levels, calculated by the ΔΔCt method, are shown on the vertical axis on a $\log_2$ scale. Orange, yellow, and green boxes indicate gene expression in 3X-40, 3X-41, and 3X-45 cells, respectively. Not applicable (N/A) data are shown as blank.

Figure 2-12 **Spatially-dependent X-ray energy deposition in the cellular nucleus.**

Chromatin located in the nuclear membrane is protected from the energy transfer caused by X-rays due to its energy interaction with the nuclear membrane (area in the blue dotted circle). Conversely, chromatin in the nucleoplasm has a high probability of being attacked by radicals, leading to the formation of basic lesions, SSBs, or AP sites (area in the red dotted circle).

CHAPTER 3: Metabolic effects

Figure 3-1 **Microscopic images of WI-38 and BJ-5ta cells on a dish.**

Primary WI-38 cells and hTERT-immortalized BJ-5ta cells are shown in the phase contrast microscopic images.

Figure 3-2 **Photographs of the sample set in the fluorescence microscope.**

The cell sample in a 35 mm dish was placed in the BZ-710X fluorescence microscope.

Figure 3-3 **Effect of 20 Gy X-ray dose on WI-38 and BJ-5ta cell proliferation.**

The number of non-irradiated and 20 Gy X-irradiated cells (seeded at 2.0×10^5 cells/well) was counted over a period of 9 days for WI-38 cells and 15 days for BJ-5ta cells. All values were normalized to the number of cells at day 0, and the error bars represent the standard deviation (SD) (n = 3). The symbol * indicates the p-value of the Student’s t-test compared to the non-irradiated and irradiated samples, respectively; *** $p < 0.001$.

Figure 3-4 **Representative microscopic images of EdU- and DAPI-stained non-irradiated (control) and irradiated WI-38 and BJ-5ta cells.**

Non-irradiated (control) and 20 Gy X-irradiated WI-38 and BJ-5ta cells were stained with EdU and DAPI and then observed under a fluorescence microscope at 20× magnification. Images of the irradiated cells were taken at 2, 5, and 9 days after irradiation. EdU (green) was added for 2 h before analysis. Cells were counterstained with DAPI (blue). The scale bar is 50 μm for all images.

Figure 3-5 **Percentage of EdU-positive cells in non-irradiated (control) and irradiated WI-38 and BJ-5ta cells.**

The percentages of EdU-positive non-irradiated (control) and 20 Gy X-irradiated WI-38 and BJ-5ta cells were obtained from EdU staining and DAPI counterstaining. Data from the irradiated cells were obtained at 2, 5, and 9 days after irradiation. EdU-positive cells were divided by the total number of cells in each microscopic field, and the fraction was multiplied by 100. Approximately 200 cells were counted in each field. The error bars represent the standard deviation (SD) ($n = 3$). Statistical analysis was performed using Student's t-test. The symbol * indicates the p-value of the t-test compared with the control and irradiated samples, respectively; *** $p < 0.001$, ** $p < 0.01$.

Figure 3-6 **Representative microscopic images of SA-β-gal-stained non-irradiated (control) and irradiated WI-38 and BJ-5ta cells.**

Non-irradiated (control) and 20 Gy X-irradiated WI-38 and BJ-5ta cells were stained with SA-β-gal and then observed under a fluorescence microscope at 20× magnification. Images of the irradiated cells were taken at 2, 5, and 9 days after irradiation. The blue color indicates the detection of SA-β-gal. the scale bar is 50 μm for all images.

Figure 3-7 **Percentage of SA-β-gal-positive cells in non-irradiated (control) and irradiated WI-38 and BJ-5ta cells.**

The percentages of the SA-β-gal-positive non-irradiated (control) and 20 Gy X-irradiated WI-38 and BJ-5ta cells were obtained from SA-β-gal staining. Data from the irradiated cells were obtained at 2, 5, and 9 days after irradiation. SA-β-gal-positive cells were divided by the total number of cells in each microscopic field, and the fraction was multiplied by 100. Approximately 70 cells were counted in each field. The error bars represent the standard deviation (SD) ($n = 3$). Statistical analysis was performed using Student's t-test. The symbol * indicates the p-value of the t-test compared with the control and irradiated samples, respectively; *** $p < 0.001$.

Figure 3-10 **Mean cell area in non-irradiated (control) and irradiated WI-38 and BJ-5ta cells.**

The mean total cell area of non-irradiated (control) and 20 Gy X-irradiated WI-38 and BJ-5ta cells were obtained from phase contrast images. Data from the irradiated cells were obtained at 2, 5, and 9 days after irradiation. The error bars represent the standard deviation (SD) ($n = 90$). Statistical analysis was performed using Student's t-test. The symbol * indicates the p-value of the t-test compared with the control and irradiated samples, respectively; *** $p < 0.001$.

Figure 3-13 **Normalized fraction of the high $\Delta\Psi$m area defined as the ratio of the red areas to the sum of the red and green areas in non-irradiated (control) and irradiated WI-38 and BJ-5ta cells.**

The red/red+green fluorescence ratios of JC-1 in non-irradiated (control) and 20 Gy X-irradiated WI-38 and BJ-5ta cells are shown. Data from the irradiated cells were obtained at 2, 5, and 9 days after irradiation, and all values were normalized to the control cells. The error bars represent the standard deviation (SD) ($n = 90$). Statistical analysis was performed using Student's t-test. The symbol * indicates the p-value of the t-test compared with the control and irradiated samples, respectively; *** $p < 0.001$, ** $p < 0.01$.

CHAPTER 4: Conclusion and future perspective

Figure 4-1 **Summary of studies on long-term effects on genes and metabolism.**

The double-lined boxes indicate new findings from this study. The study of the long-term effect of genes showed that even in the progeny of radiation surviving cells that are capable of cell division, there are DNA deletions in a patchwork pattern. Such deletions have the potential to induce chromosomal changes and shifts in altering gene expression. The study of the long-term effect on metabolism revealed an increase in both mitochondrial area and ATP levels, as well as mitochondrial activation in irreversible cell-cycle arrested cells. This suggests that ROS or SASP from irreversible cell-cycle arrested cells may damage normal surrounding cells and play a role in the development of delayed mutation. These cellular responses to radiation exposure may result in an increased carcinogenic potential.

ABBREVIATIONS

CHAPTER 1: Introduction

6-TG	6-thioguanine
DNA	deoxyribonucleic acid
DSB	double strand break
HPRT1	*hypoxanthine-phosphoribosyltransferase 1*
OH radical	hydroxyl radical
PGC-1	peroxisome proliferators-activated receptor-γ co-activator-1
PGC-1α	peroxisome proliferators-activated receptor-γ co-activator-1α
PGC-1β	peroxisome proliferators-activated receptor-γ co-activator-1β
SASP	senescence-associated secretory phenotype

CHAPTER 2: Genomic effects

AP site	apurinic/apyrimidinic site
BER	base excision repair
CNV	copy number variations
Ct	cycle threshold
CTCF	CCCTC-binding factor
D-MEM	Dulbecco’s modified Eagle’s medium
D-PBS	Dulbecco's phosphate buffered saline
EDTA	ethylenediaminetetraacetic acid
Hi-C	high-throughput chromosome capture
IDH	isocitrate dehydrogenase
LTag	large T antigen
Mb	mega base
N/A	not applicable
NHEJ	non-homologous end joining
PDGFRA	*platelet-derived growth factor receptor alpha*
qPCR	quantitative polymerase chain reaction
RT-qPCR	reverse transcription-quantitative polymerase chain reaction
SSB	single strand break

STS	sequence-tagged site
SV40	simian virus40
TAD	topologically associating domains

CHAPTER 3: Metabolic effects

AMP	adenosine triphosphate
CDK2	cyclin-dependent kinase 2
CDK4/6	cyclin-dependent kinases 4 and 6
DAPI	4′,6-diamidino-2-phenylindole (DAPI)
EdU	5-ethynyl-2′-deoxyuridine
G1	gap 1
hTERT	human telomerase reverse transcriptase
JC-1	5,5′,6,6′-tetraethyl-benzimidazolylcarbocyanine iodide
MTG	mitotracker green
NAD	nicotinamide adenine dinucleotide
NADH	nicotinamide adenine dinucleotide and hydrogen
ROS	reactive oxygen species
SAHF	senescence-associated heterochromatic foci
SA-β-gal	senescence-associated beta-galactosidase
$\Delta\Psi m$	mitochondrial membrane potential

CHAPTER 4: Conclusion and future perspectives

LNT	linear, non-threshold

CHAPTER 1: Introduction

1.1 Overview of this research

Genetic changes in cells exposed to radiation are the underlying cause of a wide variety of biological effects of ionizing radiation, including radiation-induced carcinogenesis [1]. In contrast to rapid molecular processes that occur within femtoseconds to milliseconds, such as DNA damage or DNA repair process, these biological effects develop over a relatively slow time scale of hours to days, referred to as long-term effects. These two-time scales are distinctly different; therefore, the earlier short-term molecular processes may not be predictive of the eventual long-term biological effects.

It is generally assumed that radiation-surviving cells are those that have repaired the lethal damage, such as DSBs, and have progressed through the cell cycles as seen in non-irradiated cells. However, delayed mutations and cell death have often been observed after multiple cell divisions of irradiated cells [2]. Delayed radiation effects may also be caused by irreversible cell-cycle arrest due to radiation exposure (i.e., senescence-like cells) [3]. Their specific secretions could have adverse effects on surrounding normal cells. In this study, the long-term effects of radiation on human cultured cells were investigated using a novel approach that examines two different perspectives, the genomic effects in cells in the cell cycle and the metabolic effects in irreversible cell-cycle arrested cells.

1.2 Actions of ionizing radiation in the cell

The timescale of individual cell events along one single particle track of ionizing radiation leading to biological effects is less than one second as shown in Figure 1-1. Although DNA makes up only 0.05% of the weight of the cell, it is the primary target of ionizing radiation, causing a variety of biological effects [4]. The radiolysis of water should also be focused on as a major factor in causing DNA damage, since a cell comprises approximately 70% of water. When high energy (> keV) photons or particles pass through a cell, energy is absorbed by atoms near the track and ionization or excitation occurs. The direct damage of radiation to DNA is due to this process, which develops in a time period of picoseconds [5]. In the direct effect, the radiation interacts directly with the DNA molecules by ionizing or exciting the atoms in the DNA molecule or other cellular component. These chemically active species could diffuse and react with DNA or biologically important molecules, which is called the chemical phase. The indirect effects are caused by these radicals, such as hydroxyl radical (OH radical) generally formed from water molecules, resulting in DNA damage on the timescale of picoseconds to milliseconds [6,7]. The induced DNA damage response leads to biological phases such as DNA repair. Failure of repair can lead to the cell death, which is executed by apoptosis, necrosis, mitotic catastrophe, or autophagy [8]. If DNA damage is not perfectly repaired and replication occurs, the genetic mutation may persist in the progeny of radiation-surviving cells and accumulate genomic alterations [9]. These biomolecular events typically occur on a time scale of minutes to hours. Mutated DNA damage can be inherited through generations of radiation-surviving cells, leading to genomic instability. This can lead to radiation-induced carcinogenesis, which can be observed even decades after exposure [10]. In contrast, when radiation-exposed cells undergo irreversible cell-cycle arrest, they profound phenotypic changes occur and secrete high levels of inflammatory factors that may later manifest as biological effects [11].

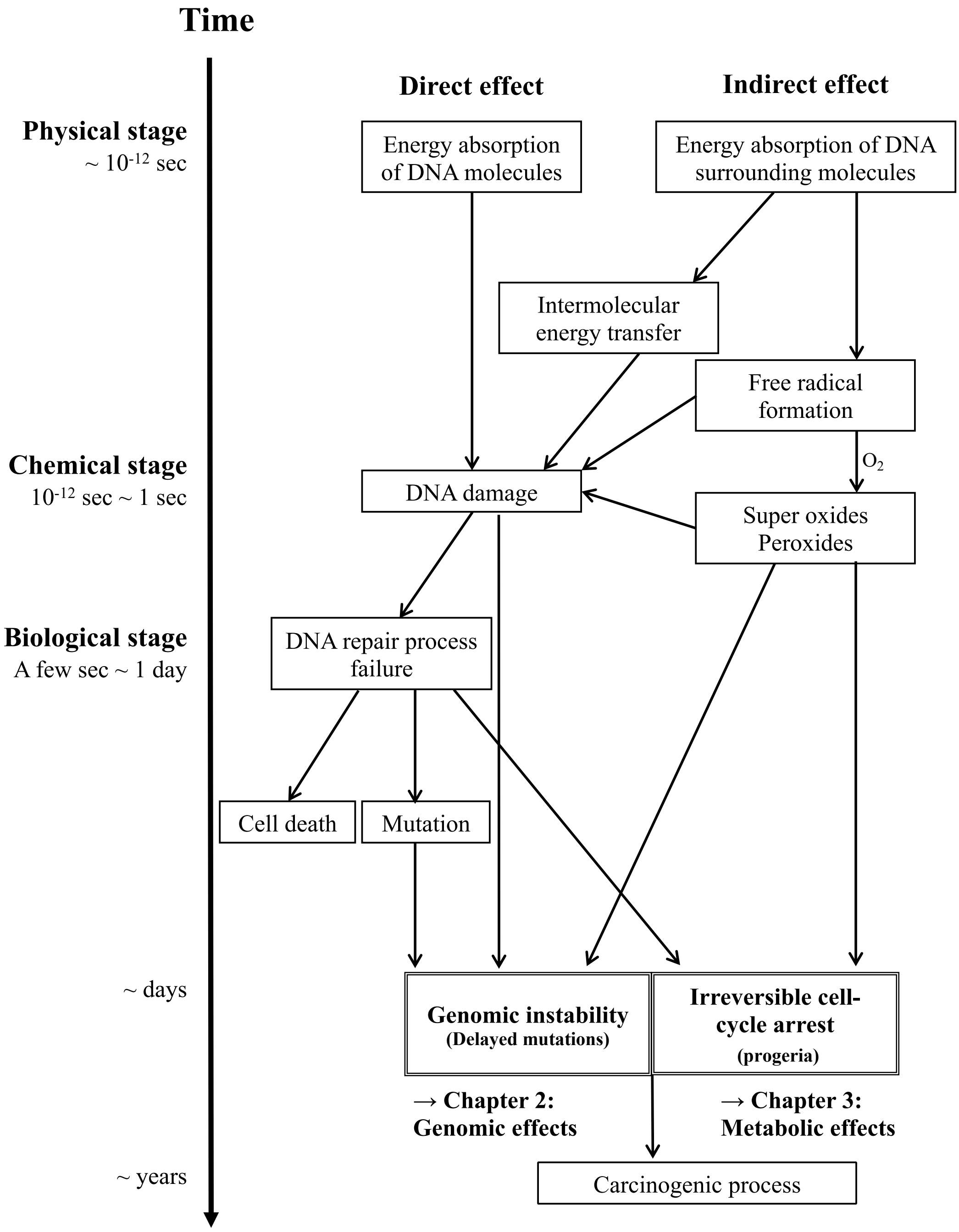

Figure 1-1. Timescale of the action of ionizing radiation in mammalian cells.

Various events in mammalian cells occur over a wide range of timescale. Direct and indirect effects of ionizing radiation can cause cell damage and resulting carcinogenesis.

1.3 Radiation-induced long-term biological effects

1.3.1 Genomic effects

Since radiation surviving cells are those that have been able to repair DSB, a lethal damage induced by radiation, all of their progeny cells are expected to have the same rate of survival as non-irradiated cells. However, when primary colonies of radiation surviving cells were collected and evaluated by secondary colony formation, a dose-dependent decrease in survival rate was observed [12,13]. These findings confirm that radiation exposure induces delayed cell death in the progeny of radiation surviving cells. Furthermore, it was reported that chromosome gaps and breaks were highly frequent in the progeny of radiation surviving cells. Dicentric chromosomes, which have two kinetochores on the same chromosome, were also observed as a delayed chromosomal aberration. Since these chromosomal aberrations are not thought to be inherited through cell division, it was concluded that these chromosomal aberrations were newly generated after multiple cell divisions after radiation exposure [14]. When mutations in the *HPRT1* gene were examined in cells derived from secondary colonies using 6-thioguanine (6-TG) resistance as an indicator, an increase in mutation frequency was observed in the progeny of radiation surviving cells, confirming delayed mutagenesis [15]. These delayed mutations are referred to as non-targeted or untargeted mutagenesis as they are not directly related to irradiation [16]. This is caused by genomic instability which is a defining characteristic of the majority of cancer cells. It increases tendency of genome mutation during cell divisions. The induction of genetic instability by radiation has been observed across a wide range of animal species, from yeast to mammalian cells, making it a universally occurring phenomenon [17].

1.3.2 Metabolic effects

Irreversible cell-cycle arrest is a permanent arrested state of cell division that is induced by pro-aging stress, including radiation-induced DNA damage. In 1956, Haff and Swim reported that normal mammalian somatic cells undergo an irreversible cell-cycle arrest after a certain number of cell divisions [18]. This report received little attention at first, but five years later Hayflick and Moorhead reported similar results using mouse somatic cells (fibroblasts), and this phenomenon was named as cellular senescence [19].

Sashin et al. demonstrated a correlation between the aging process in nuclear and aging process of mitochondria [20]. The mitochondria are often referred to as the powerhouse of the cell, as they are responsible for generating the cellular energy. Previous studies have shown that mice genetically engineered to progressively lose telomere function exhibit a number of defects attributed to cell senescence. This may result from reduced activity of peroxisome proliferators-activated receptor-γ co-activator-1α (PGC-1α) and peroxisome proliferators-activated receptor-γ co-activator-1β (PGC-1β), key factors regulating mitochondrial function. Activation of p53 as a result of telomere dysfunction plays a role in the inactivation of the mitochondrial peroxisome proliferators-activated receptor-γ co-activator-1 (PGC-1) proteins. Sahin et al. discovered that the activation of p53 directly suppresses the gene expression of the PGC-1 in mice with aberrant telomere function.

Recent studies have shown that cells undergoing irreversible cell-cycle arrest secrete a variety of bioactive substances, such as inflammatory cytokines, chemokines, extracellular matrix degrading enzymes, growth factors, and membrane vesicles (exosomes). This phenomenon is termed SASP [21], and these secretions lead to the high energy demand and mitochondrial hyperactivity. These findings suggest the potential for ionizing radiation to affect cell metabolism in the long term.

CHAPTER 2: Genomic effects

2.1 Introduction

Genomic instability, transmitted over many generations, is thought to be involved in the carcinogenic process in radiation-surviving mammalian cells [1-3]. DSBs, known as a major source of incorrect DNA repair, cause gross chromosome rearrangements resulting in structural destabilization. In particular, a large deletion (> 0.5Mb) can potentially induce genomic instability [4] and exert delayed effects including mutagenesis, lethal mutation, or reproductive death. Induced genomic instability persists for over many generations and elicit oncogenic effects [5]. More than 90% of radiation-surviving cells keep possessing mutations in their genomic DNA through 12 or more cell divisions [6]. This indicates that the initial DNA damage is transmitted through the progeny of surviving cells as "radiation signature" [7], resulting in delayed effects. The signature could activate DNA damage checkpoints in the progeny cells and lead to delayed reactivation of p53, which exhibit various phenotypes [8].

Genomic instability is generated by the spatial gene organization of topologically associating domains (TADs) [9]. The DNA mutations alter the boundaries of TADs and lead to oncogene expression, which is normally regulated by the CCCTC-binding factor (CTCF) [10]. Indeed, human isocitrate dehydrogenase (IDH) mutant gliomas establish hypermethylation at cohesion and CTCF-biding sites, which cause inactivation of TAD boundaries and activation of a cancer driver, *platelet-derived growth factor receptor alpha* (*PDGFRA*) [11]. Many studies have reported possible causes and effects of genomic instability in terms of DNA repair, cell-cycle regulation, or apoptosis [12-14]. However, little is known about the regulation of gene expression caused by genomic instability, which tends to compound in cancer cells [15].

To characterize the genomic hallmark of the progeny of irradiated cells, 6-TG resistant clones harboring a deletion of the *HPRT1* locus were isolated to determine DNA deletion sites near the *HPRT1* locus using real-time qPCR analysis with 31 general sequence-tagged site (STS) markers and 15 originally designed primers. Heterogeneous gene expression of the entire X chromosome in the progeny of radiation-surviving cells was also analyzed by both DNA microarray and real-time RT-qPCR methods. The aim of this work is to reveal the involvement of initiation and perpetuation of genomic instability in radiation carcinogenesis process.

2.2 Materials and methods

2.2.1 Cell lines and culture conditions

GM638, SV40 large T antigen (LTag)-immortalized normal human fibroblast cells, are used as parental cells as the control. GM 638 was derived from the skin of three-month-old male. The cells were obtained directly from the laboratory of Prof. Keiji Suzuki's at Nagasaki University (Nagasaki, Japan). GM638 and the progeny of radiation surviving cells (3X-40, 3X-41, 3X-45) were cultured (Figure 2-1) in high-glucose Dulbecco's modified Eagle's medium (D-MEM) (Fujifilm Wako Pure Chemical Industries, Osaka, Japan) supplemented with L-glutamine, phenol red, sodium pyruvate, 10% fetal bovine serum (Thermo Fisher Scientific, Tokyo, Japan), and Antibiotic-Antimycotic (Gibco by Life Technologies, Tokyo, Japan) at 37°C in a humidified atmosphere with 95% air and 5% CO_2. After observing the cells with an inverted microscope to confirm the degree of confluence, the cells were subcultured by the following steps: 1. Remove the complete medium. 2. Rinse cells with Dulbecco's phosphate buffered saline (D-PBS) (-) (Fujifilm Wako, Osaka, Japan). 3. Treat with 0.05% trypsin-ethylenediaminetetraacetic acid (EDTA) (1 ×) until cells detach (approximately 3 min) . 4. Add fresh complete medium.

The radiation surviving cells with a deletion at the *HPRT1* locus were selected as 6-TG-resistant clones. When cells are exposed to 6-TG, which is known to be a toxic purine analog, normal cells incorporate 6-TG through the *HPRT1* gene leading to cell death, while cells with mutation or deletion at the *HPRT1* locus do not uptake 6-TG and survive. Cells were cultured in Dulbecco's modified Eagle's medium containing 60 μM of 6-TG, for two weeks for colony growth (Figure 2-2). These *HPRT1* mutation assay was performed by Nagasaki University.

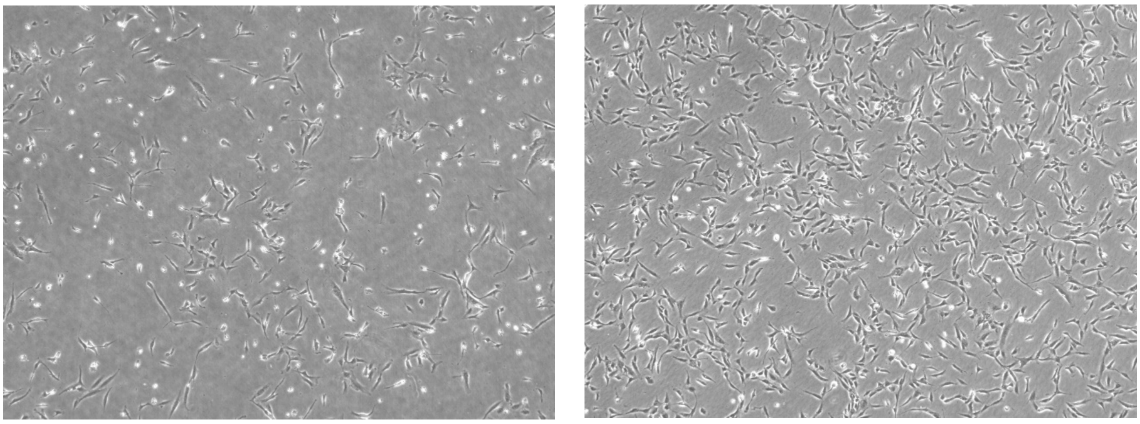

GM638 3X-40

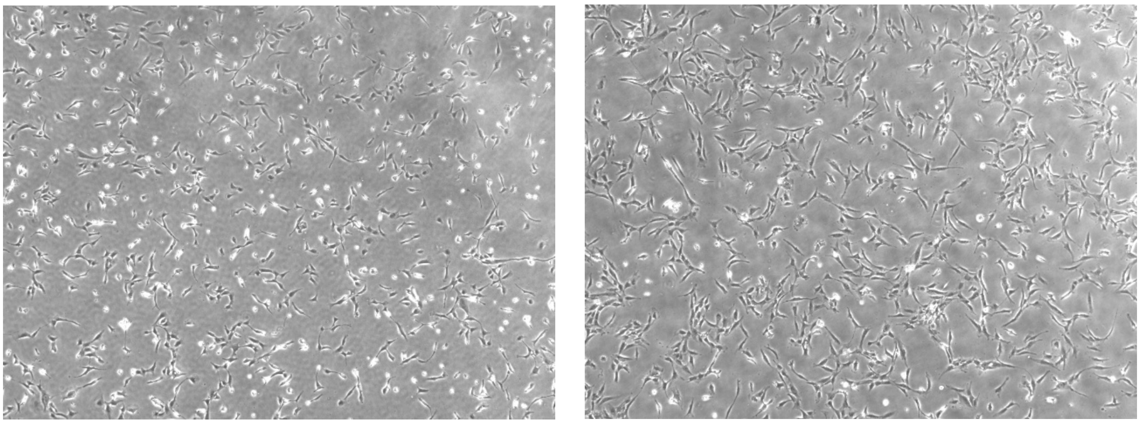

3X-41 3X-45

Figure 2-1. Microscopic images of GM638, 3X-40, 3X-41, and 3X-45 cells on a dish.

The parental cells, GM638, and its clones of the progeny of radiation surviving cells, 3X-40, 3X-41, and 3X-45 are shown in the phase contrast microscopic images.

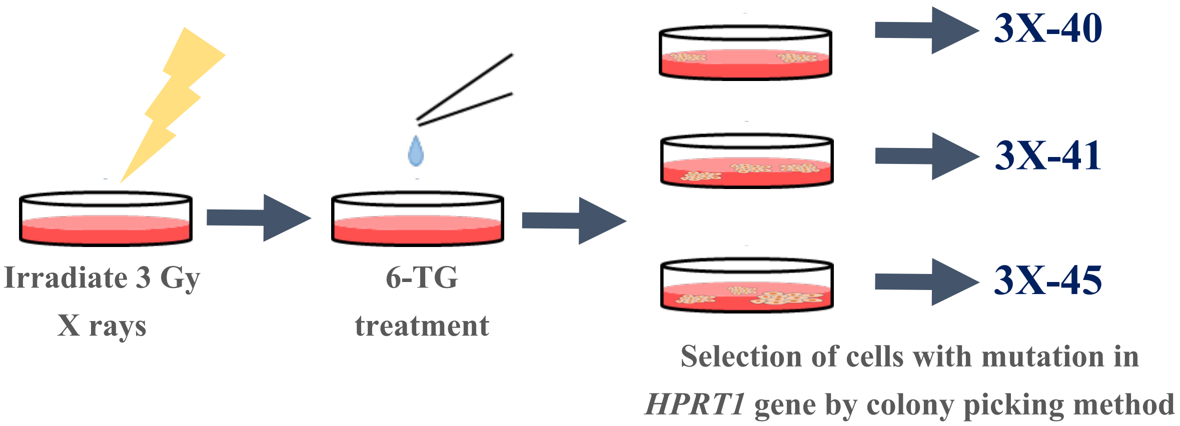

Figure 2-2. ***HPRT1*** **mutation assay procedure.**

Cells were exposed to 3 Gy of X rays and then 60 µM of 6-TG was added to obtain 6-TG-resistant clones. After two weeks of incubation, the colony-formed progeny of radiation surviving cells were randomly selected and named as 3X-40, 3X-41, or 3X-45 (performed by Nagasaki University).

2.2.2 DNA microarray

One-color microarray was used to compare gene expression between GM638 and 3X-40 cells. For target preparation, total RNAs were extracted from cells using QIAGEN RNeasy mini kit (Hilden, German). Fluorescently labelled cRNA was generated and amplified using Low Input Quick Amp Labeling Kit (Agilent, California, USA). After hybridization using the Gene Expression Hybridization Kit (Agilent, California, USA) and washing using the Gene Expression Wash Pack (Agilent, California, USA), the microarrays were scanned with the Agilent DNA Microarray Scanner. Agilent Feature Extraction software (ver.12.1.11) (Agilent, California, USA) was used to quantify the scan results. The raw data were normalized using the GeneSpring software (ver.14.9.1) (Agilent, California, USA) processed by the 75th percentile shift method. (DNA Chip Research, Tokyo, Japan)

2.2.3 qPCR

The qPCR method was used to analyze a DNA deletion pattern. Genomic DNA was isolated from each of the clones using the MonoFas DNA Cultured Cells Extraction Kit VI with Proteinase K (GL Science Inc. Tokyo, Japan). A 10 μL aliquot of the DNA solution was then used as a template for qPCR. This DNA solution was combined with a

0.8 µL solution containing either an STS marker or a designed primer pair (Table 2-1), along with 25 µL LuminoCt SYBR Green qPCR ReadyMix (Sigma-Aldrich LLC, St. Louis, MO) and 14.2 µL sterilized water to make a final volume of 50 µL. The volume of 16 µL was then added to three wells of the Eco Real-Time PCR System plate (Illumina, San Diego, CA). Finally, the plate was securely sealed with a sealing film (Figure 2-3).

The PCR was performed using the following cycling protocol: the reaction mixture was initially heated to 50 ºC for 5 s to prime for denaturation (95 ºC for 20 s), followed by 50 cycles of denaturation (95 ºC for 3 s) and annealing/extension (60 ºC, 30 s). Fluorescence intensity was monitored and recorded throughout the cycle using the Eco real-time PCR system software. Amplified gene products were confirmed and validated by melting measurement data collection, which involved increasing the temperature to 95 ºC for 15 s, 60 ºC for 30 s, and then 95 ºC for 15 s (Figure 2-4).

Table 2-1. Locations and sequences of the STS primers and newly designed primers used for qPCR analysis.

Primer	Forward 5’	Forward 3’	Reverse 5’	Reverse 3’	F: Forward sequence 5’ → 3^0 R: Reverse sequence 5’ → 3’
DXS7836	130,269,354	130,269,377	130,269,323	130,269,301	F: CATCCATGTTTTTACGATTCCTT R: GTCTCTCTGTTCGTTTTGGTATA
DXS8293	130,372,330	130,372,348	130,372,247	130,372,227	F: GGGGACTTCTGATATTTGA R: CAGTAAGGTTCTCCCTTGCTC
WI-13677	130,373,321	130,373,345	130,373,217	130,373,196	F: GTCTGGAGCCAAGAGTAATTTCATA R: TTACAGTGGGTAGTCATAGGTA
UniSTS:490481	130,385,518	130,385,537	130,384,364	130,384,345	F: CGTCTCCTCGACACCCAAGT R: TCCCCCTACTCTCGTGAACG
DXS7839	131,562,641	131,562,664	131,562,481	131,562,463	F: CTCTAACTCCTATATCGTTTATGA R: CCCTCCAACCTGAAATGAA
DXS7822	131,797,578	131,797,597	131,797,653	131,797,630	F: CCTAAGGAGCCTAACTCATC R: CCTCTAACCTTCCCTTCAAATATC
Designed primer1	131,900,775	131,900,796	131,900,863	131,900,842	F: TCACACCAAAGTCAAAGGCTGT R: TGATCTGACAAGCGATCTCCAT
DXS1298	131,900,812	131,900,830	131,900,757	131,900,739	F: CATAAACATATCGGTCACT R: CATTATCACCCTAATCTTA
Designed primer2	131,903,596	131,903,619	131,903,693	131,903,670	F: CTAAATTTTGGCTAATGTTCTGCT R: AAATGTAACCTATTTGCCATGTTT
Designed primer3	131,906,573	131,906,594	131,906,667	131,906,646	F: AGGGCGATGAATGTTTATGGAG R: CTGCTGAGCTGGATGTAGCAAT
Designed primer4	131,908,912	131,908,937	131,909,017	131,908,992	F: CGTAACAGTATTAGAGAGCCAATTTC R: TGATGGAAACAATAGTATCTTTGAGC
Designed primer5	131,911,310	131,911,331	131,911,399	131,911,378	F: ATCACCCTGGATCACCCTAATC R: CATACACCGAAAGATGGCTCAC
Designed primer6	131,912,124	131,912,145	131,912,222	131,912,201	F: TCAACTCATTTGGTTTGGTTGG R: CATCACTATAGCCAGGGAGTGC
Designed primer7	131,915,734	131,915,755	131,915,829	131,915,808	F: CTGTTACTCCACCCATTTGCTG R: GTTACTTGCTTTTGCCCAATGA

Designed primer8	131,916,386	131,916,407	131,916,475	131,916,454	F: AACAGACATCGGGCATCATATC R: TGTTGGATTTGGAAGTGGTTTG
Designed primer9	131,917,644	131,917,667	131,917,743	131,917,720	F: GCAGGCTGCTGGTGTTTCTCATTC R: TGGGTGGGAGAAGAGAGATGCAGT
Designed primer10	131,919,079	131,919,100	131,919,177	131,919,156	F: CATGCTGGCTTCAGTTATGACC R: TCCCCTTTATTCATCCCTCTCC
Designed primer11	131,923,303	131,923,324	131,923,394	131,923,373	F: GGAAGCTGAAGGTCTGTTTGTG R: TTCCTTTACCCCTGCATTTCAC
Designed primer12	131,929,536	131,929,557	131,929,617	131,929,596	F: GTGCAGGGTCATATAGGTGTGG R: TGGAAATATTGATGACCCATCG
Designed primer13	131,931,891	131,931,912	131,931,980	131,931,959	F: AAAGGAACGTCTTGTCCCATTG R: ACCTGAAGCAGAAGTGGCTTTC
Designed primer14	131,934,041	131,934,063	131,934,121	131,934,100	F: CAAGAAATGTCTGGCTTTTCCAC R: CACCCTTTTCCTTGCCTAATTG
Designed primer15	131,934,798	131,934,819	131,934,877	131,934,856	F: ATTTTCAGGCTGCAACAGACAC R: TTCAGTCCCACATTCTTTCCAG
AL023941	131,935,200	131,935,221	131,935,095	131,935,074	F: CGGGAGTGTATGGAACTTCTCA R: ACCTATGAGTCTTCGACCAAAC
AL023940	131,937,574	131,937,595	131,937,466	131,937,445	F: CCGAACCTCTGATGTCTCCTCT R: ACTCGGTCCTGAGGAATCTTAA
AL023953	131,938,395	131,938,416	131,938,335	131,938,316	F: GTGAAAAAGAGAGGAAAGAACG R: AAGGAACCAAAAGTTACGTT
AL035152	132,036,647	132,036,666	132,036,814	132,036,793	F: CGACTTGCTTCCTCTTCAGG R: TCATGTGCAATACACATTGAGG
WI-11835	132,075,902	132,075,926	132,075,823	132,075,799	F: ACAAAATCCCCAAAACTTTTATTTA R: GCAATTGTGTTGTAAAGTTTCAAAT
DXS6808	132,103,464	132,103,486	132,103,717	132,103,695	F: ATCCTGATATCTGCCTTTAAATG R: GGTATATAACAATTGTTGGTGCA
DXS7405	132,209,532	132,209,556	132,209,459	132,209,441	F: GAATGACTATAATAGAAGACTTAAC R: CGGTTAGAATCTTTGTAGT
DXS7457	133,125,986	133,126,006	133,125,951	133,125,932	F: CACTTATAAACGAGGAAACGG R: CAGACCCTTCATTTTCTAGG

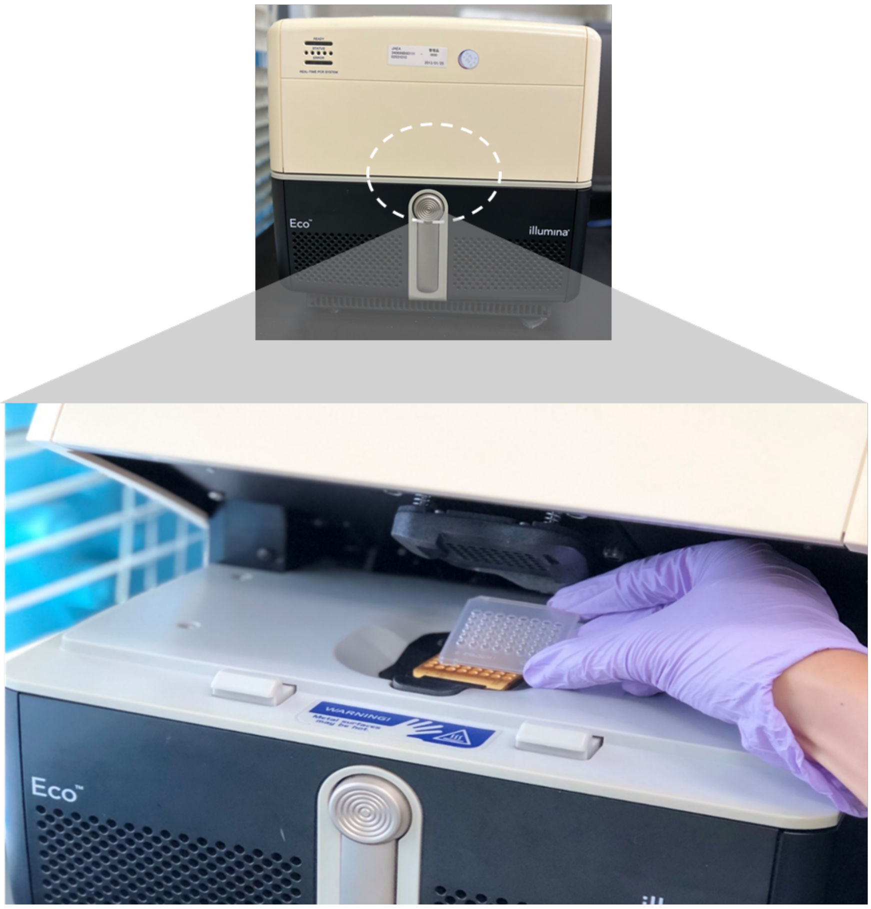

Figure 2-3. Photographs of the sample being inserted into the real-time PCR system.

Samples were loaded into a 96-well plate and inserted into the Eco Real-Time PCR System, Illumina.

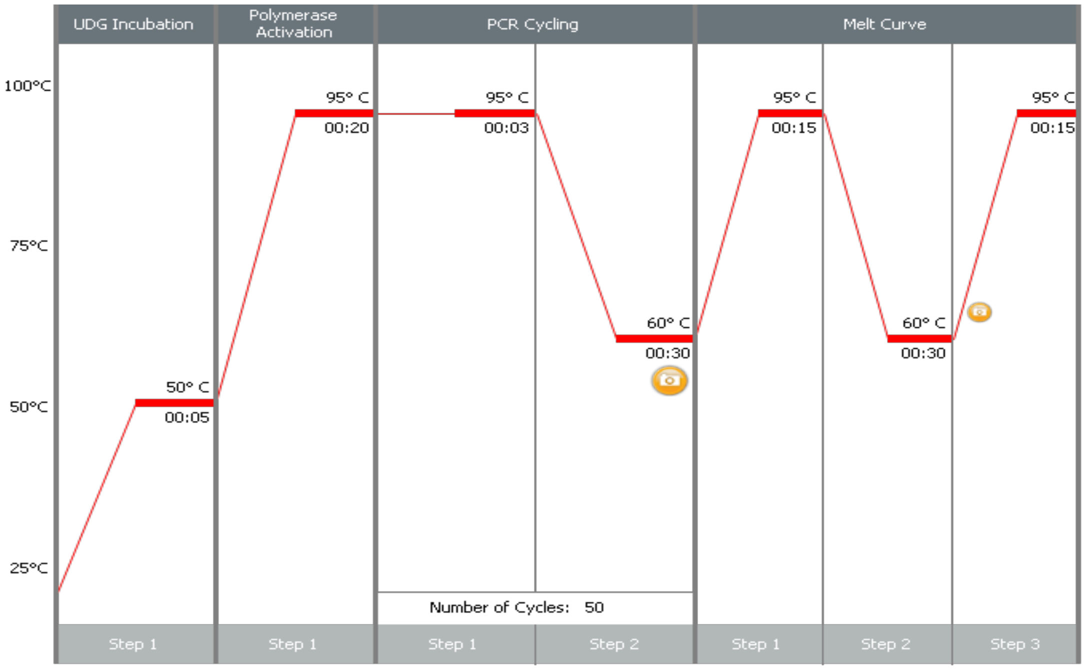

Figure 2-4. Thermal cycling profile for qPCR analysis.

The PCR reaction mixture was initially heated at 50 ºC for 5 s, followed by initial denaturation at 95 ºC for 20 s. The PCR cycling consisted of denaturation at 95 ºC for 3 s and annealing/extension at 60 ºC for 30 s. The number of amplification cycles was set to be 50. The melting curve was then analyzed according to the following protocol: 95 ºC for 15 s, 60 ºC for 30 s, and 95 ºC for 15 s.

2.2.4 Gel electrophoresis

Sometimes more than one DNA product is copied in a PCR experiment. In such cases, electrophoresis on a 2% agarose gel is used to confirm a single band in the gel, indicating that only the specific sequence of interest has been copied. If more than one sequence was copied, these STS markers or PCR primers were not used for further experiments (Figure 2-5).

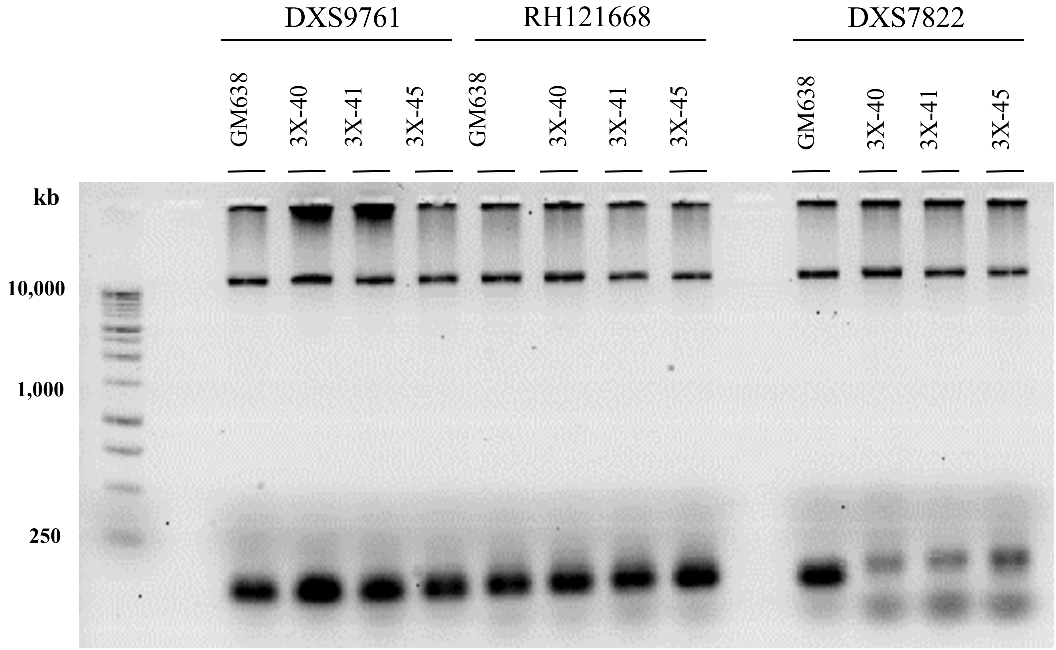

Figure 2-5. Agarose gel electrophoresis image of qPCR products.

One of the typical agarose gel electrophoresis images used to validate qPCR products is shown. Unexpected bands were visualized with the product of a DXS7822 primer pair against 3X-40, 3X-41, and 3X-45 clones. These STS primers were not used in further experiments.

2.2.5 RT-qPCR

Total RNA was extracted from each clone using a RNeasy Plus Mini kit (QIAGEN, Hilden, German), and then cDNA was synthesized using a QuantiTect Reverse Transcription Kit (QIAGEN, Hilden, German). One µl of cDNA solution were mixed with a 0.3 µl solution containing a primer pair (Table 2-2), 25 µl of SsoAdvanced Universal SYBR Green Supermix (Bio-Rad, California, USA), and 23.7 µl of nuclease free water. An aliquot of the liquid (15 µl, sufficient for three wells) was added to each well of the plate specific to the Eco Real-Time PCR system (Illumina, San Diego, CA). Sealing film was then attached to the plate.

PCR was performed with the following cycling process. The reaction mixture was heated to 50ºC for 2 min to prepare for initial denaturation (95ºC for 30 s), followed by 50 cycles of denaturation (95ºC for 15 s) and annealing/ extension (60ºC, 30 s). Fluorescence intensity was recorded during the cycle using the software of the real-time PCR system. Real-time PCR data were verified by melt curve analysis, measured by the temperature increases of 95ºC for 15 s, 65ºC for 30 s, and 95ºC for 15 s (Figure 2-6).

Table 2-2. Locations and sequences of primers used for RT-qPCR analysis.

Cytoband	Gene name	qPCR primers	Remarks
Xp22.33	MXRA5	F: GACGCGCTCTTCAGTTTTGA R: ATCTCCGGCATCTTTGTCCG	Matrix remodeling associated 5, cancer-related gene
Xp22.2	SHROOM2	F. AGAGCCTCGCGGACTATGA R: GGGCTGAAGGCTGTCCAATAA	Shroom family member 2, PDZ domain containing gene
Xp11.3	MIR221	F: ATCCAGGTCTGGGGCATGAAC R: GGTAGCCTGAAACCCAGCAGA	miRNA
Xp11.22	GSPT2	F: CATCTGCCTCGAGACGTTCA R: TGCTGTCAATTCTCCTCACAGTA	G1 to S phase transition 2, eukaryotic peptide chain release factor GTP-binding subunit ERF38
Xq11.2	ZC3H12B	F. CACCCTCTCGTTCTATGCCG R: TGGTGGTTCCTGAAGGTTGG	Zinc finger CCCH-type containing 12B, probable ribonuclease
Xq13.1	DLG3	F: CGGCCTCGACGTGATATTGA R: CAGTGCTTGCCCCTCTCTG	Discs large MAGUK scaffold protein 3 Drosophila tumor suppressor gene, discs large (Dia) homolog 3
Xq21.11	HMGN5	F. GATATGAGGCAGGAGCCAAAGA R: TCTTGCTTGGTTTCAGCAACTG	High mobility group nucleosome binding domain 5, modulates cellular transcription
Xq22.1	ARMCX2	F: ACACTGGGGCTATACCGAAAG R: GACCTGGTTACACCCTTGCC	Armadillo repeat containing X-linked 2, contain multiple armadillo repeats
Xq22.11	PHEX	F: GCACGATCCTCTTTCTAGTGAGTC R: TCACAAGCGAACCGGAAGAA	Phosphate regulating endopeptidase X-linked, zinc metallopeptidase
Xq23	PAK3	F: GATAGGCGAGGATCTGCCAAG R: GCTTCCTTTGCAGCGATAATCA	p21 (RAC1) activated kinase 3
Xq26.1	MIR503HG	F: TTCCTGAAAGACCAAGCCCG R: TGGAGATGCTGGATGCCTTC	downstream effector of CDC42 and RAC1 IncRNA
Xq28	GABRA3	F: AAATCCGTGGAAGTGGCACA R: CGCTTGAGATGGAAGTGGGT	Gamma-aminobutyric acid type a receptor subunit alpha3, mediating inhibitory neurotransmission

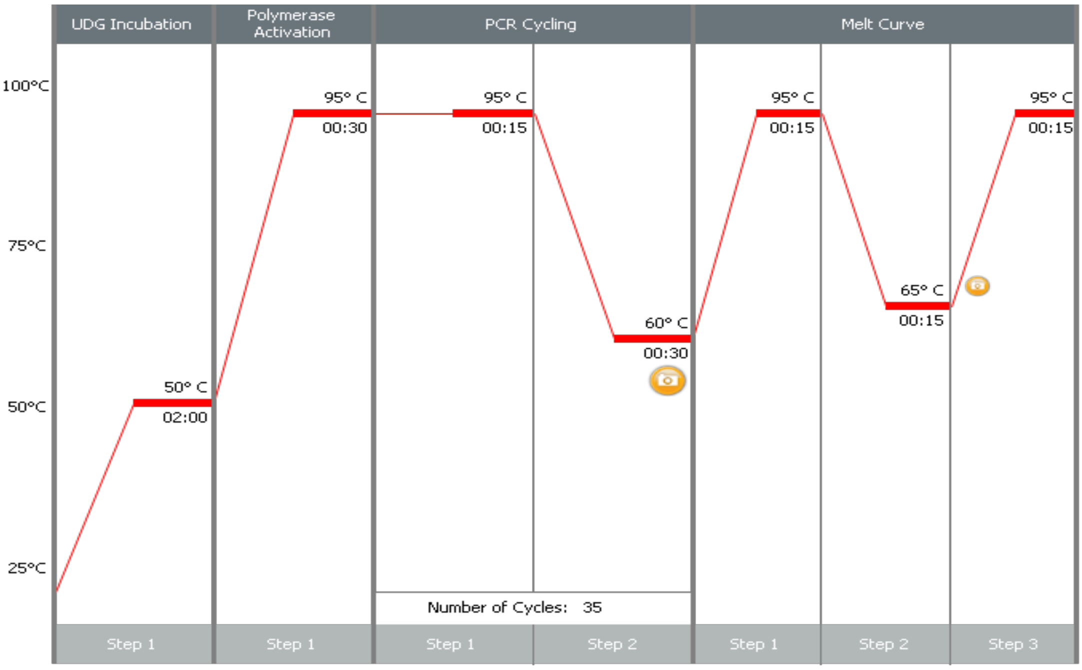

Figure 2-6. Thermal cycling profile for RT-qPCR analysis.

The PCR reaction mixture was initially heated at 50 ºC for 2 min, followed by initial denaturation at 95 ºC for 30 s. The PCR cycling consisted of denaturation at 95ºC for 15 s and annealing/extension at 60 ºC for 30 s. The number of amplification cycles was set to be 35. The melting curve was then analyzed according to the following protocol: 95 ºC for 15 s, 60 ºC for 15 s, and 95 ºC for 15 s.

2.2.6 Evaluation of PCR assay

The qPCR data were evaluated using cycle threshold (Ct) values and melting curve analysis. The Ct value is the number of cycles at the threshold level of log-based fluorescence. It indicates the number of PCR cycles required to copy the DNA to be detected. High Ct values (> 35) indicate the presence of DNA-deletion at the site where the primer anneals. The melt curve analysis is for confirming the single specific product of PCR. Finding multiple melting curve peaks indicates that the PCR product is non-target DNA, such as unspecific primer dimers (Figure 2-7).

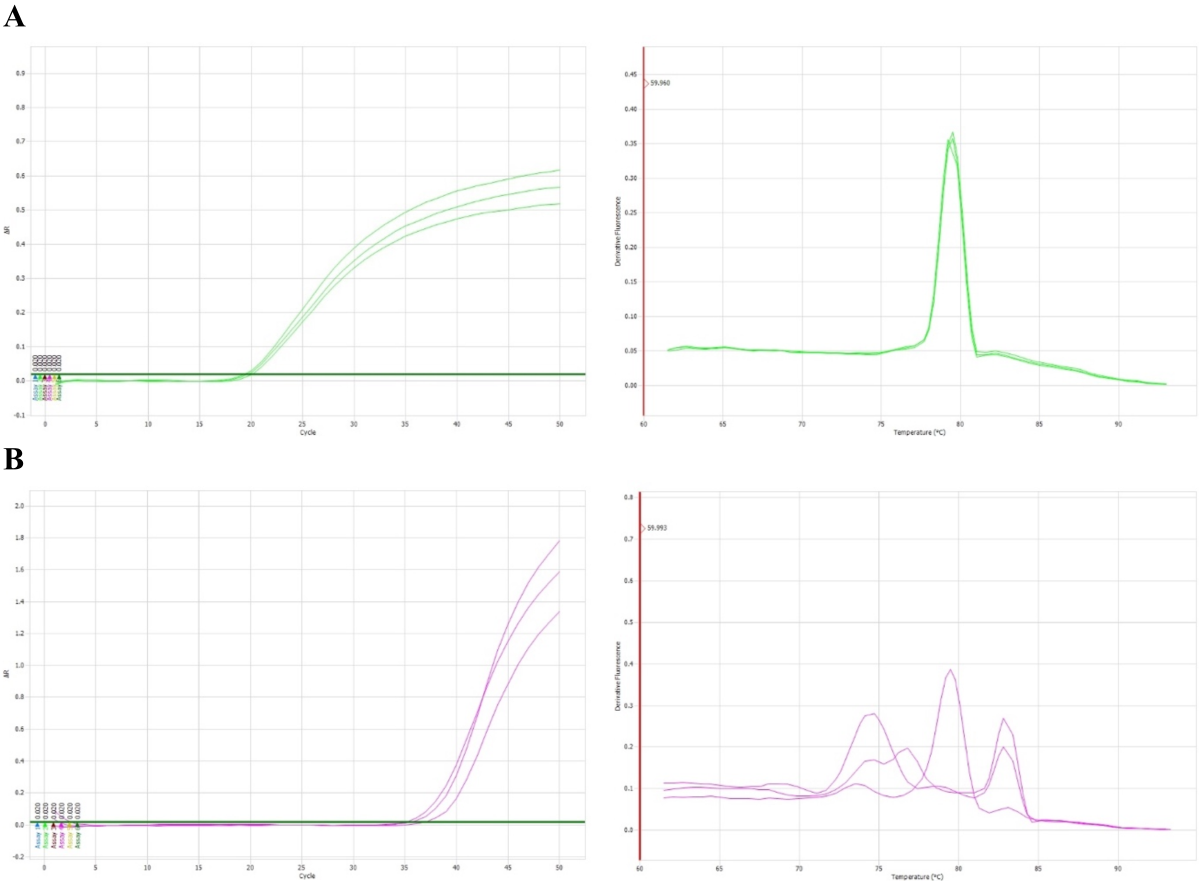

Figure 2-7. Positive and negative results of qPCR analysis.

One of the positive and negative results of amplification and melting curves are shown. Left: The horizontal axes represent the number of PCR cycles, and the vertical axes represent the fluorescence intensity. Right: The horizontal axes represent the temperature, and the vertical axes represent -ΔF/ΔT (fluorescence change/temperature change). The samples were divided into three wells of a 96-well plate, and the results are represented by three lines.

(A) Positive results obtained with the DXS7888 primer against 3X-40 clones are shown. Left: The mean value of Ct was 19.69. Right: A single peak was observed by melting curve analysis.

(B) The negative results obtained with the DXS7888 primer against 3X-41 clones are shown. Left: The mean value of Ct was 35.89. Right: The observed multiple peaks of the melting curves were not consistent among the three observations.

2.2.7 Calculation of gene expression level

Data from RT-qPCR experiments were analyzed with using the ΔΔCt method to obtain the relative gene expression values. The mean Ct values and their standard deviations were obtained from the Eco Real-Time PCR System firmware (ver. 4.0.07.0). The following table represents one of the ΔΔCt calculations (Table 2-3).

Table 2-3. *MARA5* expression level in 3X-40 cells, calculated by the ΔΔCT method.

Clone	*MARA5* mean Ct±SD	*ACTB* mean Ct±SD	ΔCt	ΔΔCt	FC	Log_2 FC
GM638	25.76 (±0.03)	20.64 (±0.25)	5.12	-	-	-
3X-40	28.25 (±0.20)	21.26 (±0.23)	6.99	1.87	0.27	-1.87 (±0.40)

First, ΔCt is defined as the difference between the mean Ct values of the target and endogenous genes as follows:

$$\Delta Ct \equiv Ct_{\,target\ gene} - Ct_{\,endogenous\ gene}\,.$$

Then, the ΔCt value for GM 638 (the control) is calculated as

$$\Delta Ct_{\,GM638} = Ct_{\,MARA5} - Ct_{\,ACTB} = 25.76 - 20.64 = 5.12\,.$$

Similarly, the ΔCt value for (the test sample, i.e., progeny of irradiated cells of) 3X-40 is given as

$$\Delta Ct_{\,3X-40} = 28.25 - 21.26 = 6.99\,.$$

Second, ΔΔCt is calculated by subtracting ΔCt of the control from ΔCt of the test sample (i.e., progeny of irradiated cells).

$$\Delta\Delta Ct \equiv \Delta Ct_{\ test\ sample} - \Delta Ct_{\ control}$$

$$\Delta\Delta Ct = \Delta Ct_{3X-40} - \Delta Ct_{GM638} = 6.99 - 5.12 = 1.87$$

Third, the fold change (FC) is calculated as shown below.

$$FC_{\ 3X-40} = 2^{-\Delta\Delta Ct} = 2^{-1.87} = 0.27$$

Finally, the log base 2 of the ΔΔCt value is taken to even out the scales of up and down regulated genes. Otherwise, up regulated genes have a scale of 1 to infinity, while down regulated genes have a scale of 0 to 1.

$$\log_2(FC_{\ 3X-40}) = \log_2(0.27) = -1.87$$

The variance of the ΔΔCt is calculated as the standard deviation (SD). For example, the standard deviation of the fold change is calculated as the square root of the sum of the squared standard deviations, as shown below.

$$SD_{\log_2 FC}$$

$$= \sqrt{(SD_{MARA5\ vs.3x-40})^2 + (SD_{MARA5\ vs.GM638})^2 + (SD_{ACTB\ vs.3X-40})^2 + (SD_{ACTB\ vs.GM638})^2}$$

$$= \sqrt{0.20^2 + 0.03^2 + 0.23^2 + 0.25^2}$$

$$= 0.40$$

2.3 Results

2.3.1 DNA deletion pattern

The three cells with the large deletions (3X-40, 3X-41, and 3X-45) were selected for the qPCR analysis compared to those of the parent cell (GM638), as well as two spontaneous mutant clones (X0-1 and X0-2) and two 3 Gy X-ray induced point mutant clones (3X-2 and 3X-21). The entire HPRT1 exon was retained in all cells analyzed. STS markers and 15 PCR primer pairs were set in a relatively small region around 132 and 135 Mb of the X chromosome (Figure 2-8).

The analysis of qPCR was applied only to regions 1 and 2 for the X0-1, X0-2, 3X-2, and 3X-21 clones, where the markers and primers were closer together than in other regions. These point mutant clones were positive for the markers and primers tested, indicating that there were no deletions in these regions. In contrast, contrary to initial expectations, the deletion site was not located in a single region containing the *HPRT1* locus. The boundary between the deletion site and the remaining original DNA was indistinct, and the PCR negative sites were distributed in a patchwork pattern. The results shown in region 1 indicate that target PCR products were detected from primer 8 to primer 13 against 3X-40, 3X-41, and 3X-45. The deletion pattern of 3X-45 in region 1 was similar to that of 3X-40 and 3X-41, but the STS markers near the *HPRT1* locus (WI-

11835, DXS 6808) were positive while 3X-40 and 3X-41were negative. As shown in region 2, PCR-negative sites were distributed in a patchwork pattern.

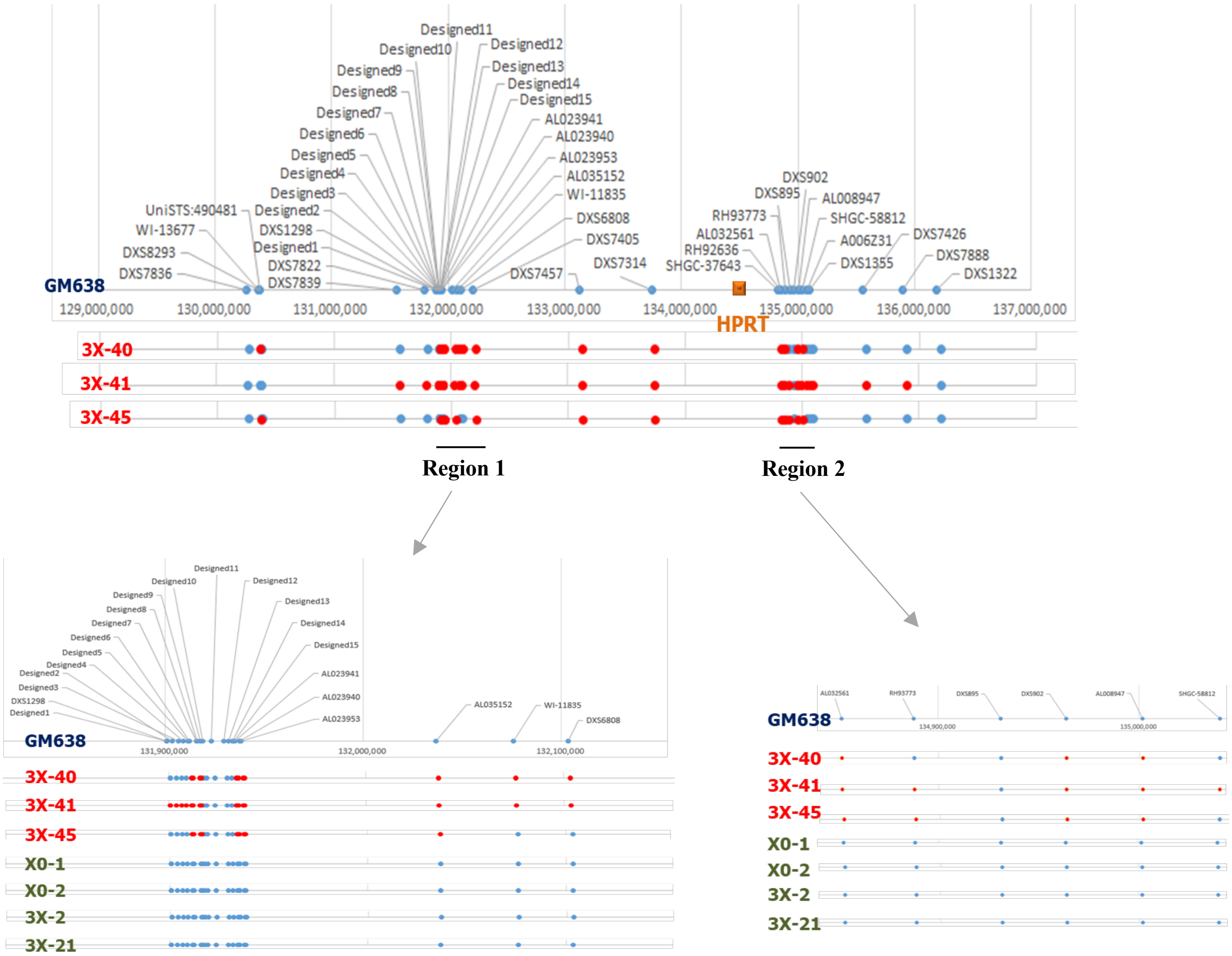

Figure 2-8. DNA deletion in a patchwork pattern.

Results of qPCR using 21 STS primers and 15 newly designed primer pairs (named as Designated 1-15) against clones. Clone GM638 is the control (parent cells). Clones 3X-40, 3X-41, and 3X-45 are the progeny of radiation surviving cells with large DNA deletions. X0-1 and X0-2 are spontaneous mutant clones. 3X-2 and 3X-21 are 3 Gy X-ray induced point mutant clones. The entire *HPRT1* exon is present in all cell types. The genomic region located on the X chromosome from 130 to 137 Mb was examined. Positive and negative PCR results are shown as blue and red dots, respectively. The *HPRT1* locus is shown as an orange box. The enlarged figures of region 1 and region 2 are shown at the bottom of the main figure.

The three cells with the large deletions (3X-40, 3X-41, and 3X-45) were selected for the qPCR analysis compared to those of the parent cell (GM638), as well as two spontaneous mutant clones (X0-1 and X0-2) and two 3 Gy X-ray induced point mutant clones (3X-2 and 3X-21). The entire HPRT1 exon was retained in all cells analyzed. STS markers and 15 PCR primer pairs were set in a relatively small region around 132 and 135 Mb of the X chromosome (Figure 2-8).

2.3.2 Differential gene expression

The $\log_2$ fold change values of 3X-40 cells (progeny of surviving cells) were obtained from a microarray assay and presented as relative to the control, GM638 cells (parental cells as the control) (Figure 2-9). Genes near the *HPRT1* locus showed significantly negative fold changes compared to other distant genes. All genes with the value of $\log_2$ fold changes lower then −8 were localized near the *HPRT1* locus, 130Mb-135Mb on X-chromosome.

Figure 2-9. Microarray analysis of gene regulation on the X chromosome in 3X-40 cells.

Microarray results are presented as fold change of gene expression levels on the X chromosome in 3X-40 cells relative to the control, GM638 cells. The horizontal axes represent the genomic coordinates using the human genome sequence (GRCh37), and the vertical axes represent the fold change in gene expression level on a $\log_2$ scale. The blue circles represent genes that show a 2-fold or greater increase in expression level (up-regulated) compared to the control, while the red circles indicate genes that show a 1/2-fold or less decrease in expression level (down-regulated) compared to the control. The gray circles indicate genes with no significant difference from the control. The *HPRT1* locus is shown as a green circle.

The numbers of up- and down-regulated genes on the X chromosome of 3X-40 cells, obtained from the microarray assay, were counted (Figure 2-10). Regulated genes were not restricted to the area around the *HPRT1* locus but were distributed over the entire X chromosome. Up-regulated genes, indicated by the blue line, showed repeated peaks, and the peak height appeared to be similar. Down-regulated genes indicated by the orange line also showed repeated peaks, but the peak height was the largest at the location of the *HPRT1* locus and gradually decreased with gene distance from the *HPRT1* locus.

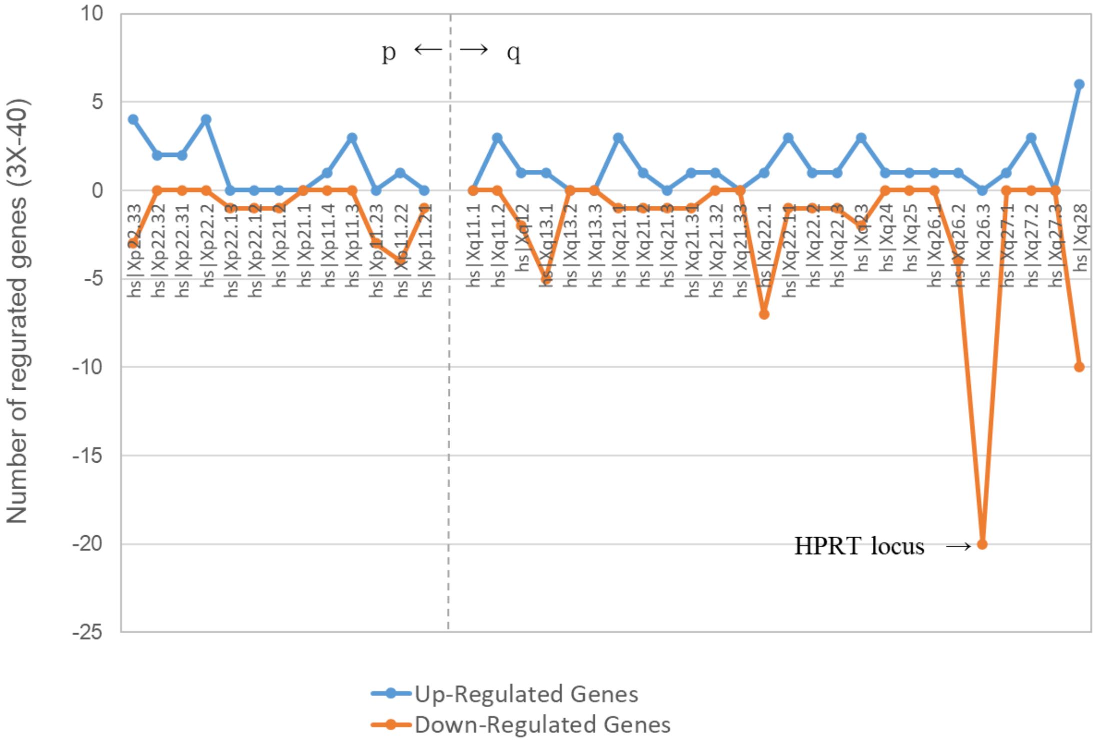

Figure 2-10. The number of regulated genes of the X chromosome in 3X-40 cells determined by microarray analysis.

The horizontal axis represents the X-chromosome bands arranged in order of gene location from upstream (left) to downstream (right), and the vertical axis represents the number of regulated genes. A minus sign (-) is given to the number of down-regulated genes. The blue and orange lines are drawn by connecting the points plotted by the number of up- and down- regulated genes, respectively.

Twelve genes were selected from the results of 3X-40 from the microarray analysis and their $\log_2$ fold change values were analyzed by RT-qPCR with other progeny of radiation surviving cells, 3X-41 and 3X-45 (Figure 2-11). The expression pattern of each gene was mostly consistent with the results from the microarray assay, and most of the tested genes showed similar trends of up- or down-regulation as typically seen for *MIR221*, *HMGN5*, *PHEX*, *MIR503HG*, or *GARBA3*. However, some of the genes had different regulated levels among the mutant clone cells, and furthermore, some genes showed contradictory expressions as seen in *DLG3*, *ARMCX2*, or *PAK3*.

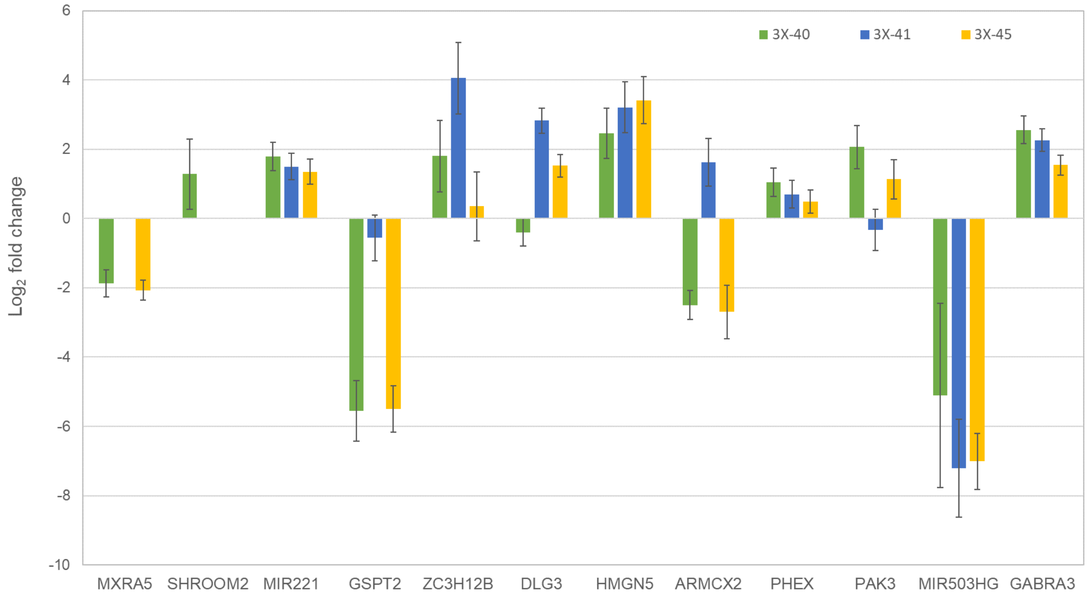

Figure 2-11. RT-qPCR analysis for the twelve genes selected from the microarray analysis. One gene per peak in Figure 2-10 was randomly selected for RT-qPCR analysis. All data were normalized to the reference gene, *ACTB (actin beta)*, and expressed as relative to the control, GM638 cells. Gene symbols (locations and sequences of primers are shown in Table 2-2) on the horizontal axis are arranged in the order of gene location from upstream (left) to downstream (right) of the X chromosome. The fold change of gene expression levels, calculated by the ΔΔCt method, are shown on the vertical axis on a $\log_2$ scale. Orange, yellow, and green boxes indicate gene expression in 3X-40, 3X-41, and 3X-45 cells, respectively. Not applicable (N/A) data are shown as blank.

2.4 Discussion

The findings demonstrated that the deletion patterns among the three mutant clones examined were dissimilar yet partially comparable. Although the three mutant clones were established independently, it is noteworthy that they exhibit a similar patchwork pattern both upstream and downstream of the *HPRT1* locus. This suggests that both the structure of the X chromosome within the cell nucleus and radiation tracks play a role in the generation of large deletions with complex neighboring structures. Chromosomes are known to possess a unique three-dimensional structure characterized by large loops, the bases of which are anchored in a scaffold-like structure [16]. Such loops are likely to be susceptible to ionization and excitation by free radicals generated by radiation and water radiolysis (Figure 2-12).

Another mechanism that can cause patchwork-like deletions is non-DSB-type clustered DNA, such as AP sites, caused by base lesions, SSBs, AP sites, or ionization or excitation of both chromosomes and water in a single radiation track. These clusters of base lesions may be converted to additional DSBs by BER proteins, particularly glycosylases or AP lyase [17-20]. The additional DSBs are not a direct result of the initial DNA damage, but rather the result of an attempt to repair the damage, which would be considered a false repair. The two-step process may result in large deletions induced around the *HPRT1* locus. First, two (or more) DSB generated directly by radiation are mis-rejoined by nonhomologous end joining (NHEJ) or alternative end-joining pathways, and then additional DSBs are induced by the action of BER enzymes. The latter DSBs could also induce mis-rejoining, eventually forming a patchwork deletion pattern.

Although the biological significance of this patchwork DNA deletion pattern is not clear, it is believed that the resulting structural variation will inevitably lead to structurally unstable chromosomes. Indeed, previous studies have shown that delayed chromosome instability occurs in X chromosomes with large deletions. The present study reveals a complex pattern of deletions that may be responsible for chromosomal aberrations associated with carcinogenesis.

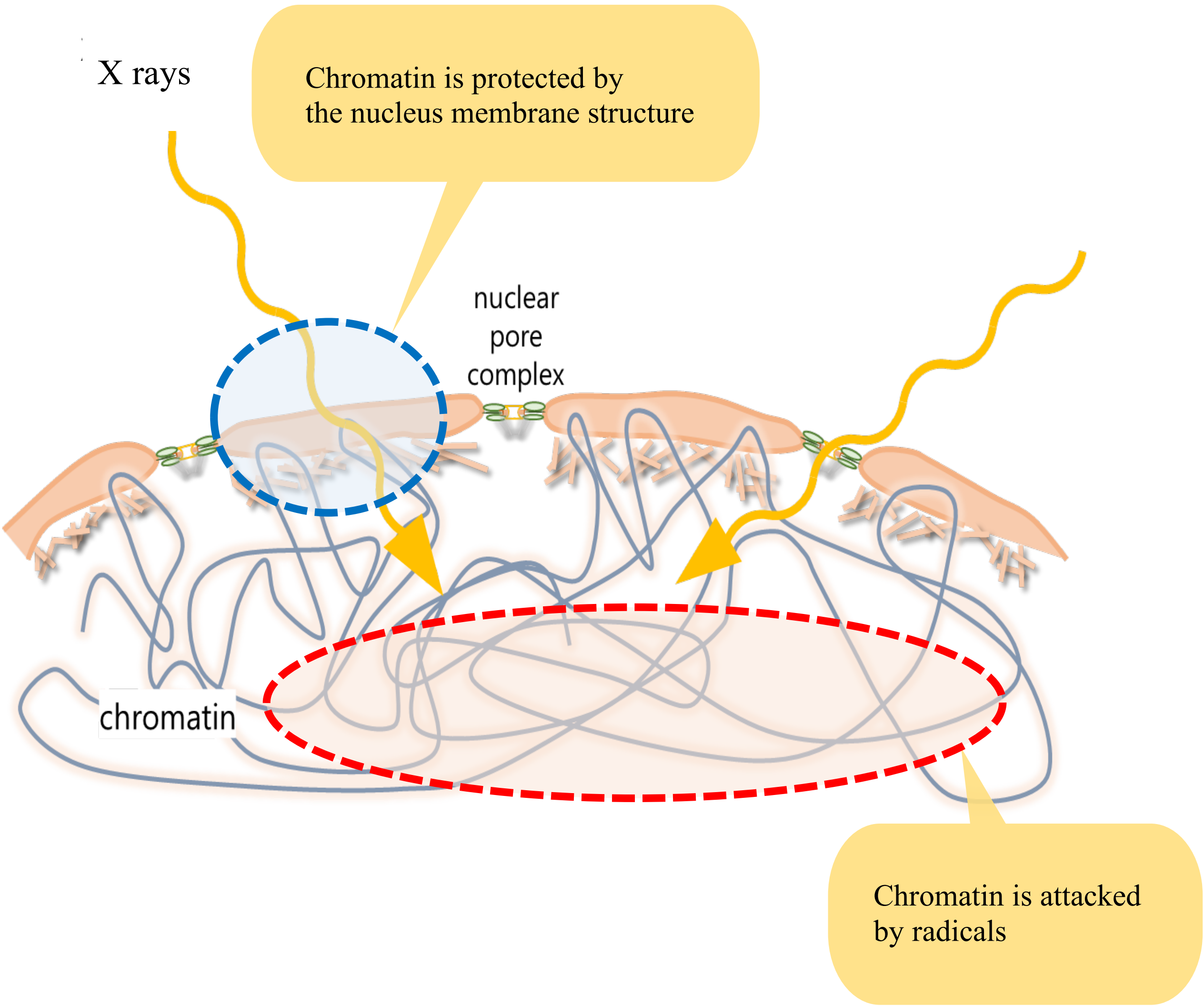

Figure 2-12. Spatially-dependent X-ray energy deposition in the cellular nucleus.
Chromatin located in the nuclear membrane is protected from the energy transfer caused by X-rays due to its energy interaction with the nuclear membrane (area in the blue dotted circle). Conversely, chromatin in the nucleoplasm has a high probability of being attacked by radicals, leading to the formation of basic lesions, SSBs, or AP sites (area in the red dotted circle).

The genetic and epigenetic mechanisms underlying genomic instability due to a patchwork deletion pattern were investigated. In the microarray analysis data, the level of down-regulated genes in a region of 130-135Mb of the X chromosome, where the *HPRT1* locus is located, was significantly lower than other down-regulated genes (Figure 2-9). This was due to the large deletion around the *HPRT1* locus [21].

The numbers of down-regulated genes were shown as repeated peaks (Figure 2-10), and the peak heights were dependent on the distance of the gene location from the *HPRT1* locus, suggesting that the genes closer to the large deletion site around the *HPRT1* locus are more likely to be affected than the distant genes. The down regulations are not presumed to be caused by DNA deletion. Since it is generally accepted that ionizing radiation of 1 Gy causes approximately 40 DSBs in mammalian cells [22], the dose of 3Gy in the present study randomly causes 120 DSBs in the whole genome of a cell; thus, other deletions originating from DSBs in the X chromosome scarcely cause the down regulations of the genes. These results indicate that the large deletion of the *HPRT1* locus causes ripples over the entire X-chromosome, presumably through certain types of epigenetic regulation, not just in the long arm of the X chromosome where the *HPRT1* locus is located. This is consistent with the demonstration in a previous study that genetic variants affect distal gene expression through association with CpG methylation [23].

The number of up- regulated genes also showed characteristic repeated multiple peaks (Figure2-10), where the peak height, namely the number of up-regulated genes, was typically identical. According to the report of chromotheripsis, which is frequently identified by the cancer genome sequencing, the DNA repair process for DSBs attempts to rearrange chromosomes [24], but hundreds of different mutations are induced in the chromosome after the repair process if the damage is profound. These induced mutations can cause DNA duplications, deletions, inversions, or copy number variations (CNVs) and other alterations [25]. The up- or down-regulation of the entire X chromosome in the progeny cells may be due to the chromosome rearrangement that occurred in the parental cells, suggesting that the progeny of radiation exposed cells harboring “radiation signature” may have radiation-specific gene regulation that would be different from that of normal cells.

One gene in each peak of up- or down- regulated gene number from Figure 2-10 was randomly selected to set a primer of RT-qPCR to investigate whether the gene regulations were induced not only in 3X-40 cells, but also in other progeny cell lines, 3X-41 and 3X-45. The results of RT-qPCR analysis indicated that the tested genes showed similar trends of up- or down-regulations (Figure 2-11). It should be noted that not applicable (N/A) data, shown as blanks, indicate that the gene is expressed at very low levels for detection by RT-qPCR. A common gene regulation mechanism operating in the three *HPRT1* gene mutant cell lines would be strongly associated with a change in chromatin structure, such as TADs in the parental (X-ray exposed) cells. Some different or contradictory gene expression levels among the mutant clones are also interpreted from TAD structure. TADs are organized into two separate compartments: A, corresponding to open chromatin, and B, corresponding to closed chromatin [26,27]. If the compartments are not altered, the level of up- or down-regulation would be similar in mutant cells. However, the induction of the compartment changing are also thought to be occur coordinately with replication timing by boundary shifting during cell differentiation [28]. This suggests that the A/B compartment, which changes during cell differentiation or cell-cycle progression, might be an origin of the contradictory gene expressions in the progeny of radiation surviving cells. Since the TAD compartment boundary disruption in human cancer cells misguides gene expressions [29], the progeny cell-specific gene expression may work as a key to reveal carcinogenesis. To elucidate the mechanism underlying gene regulation in radiation-surviving cells, future research is needed. In particular, the Monte Carlo simulations of X-ray track structure should be performed to reveal complex DNA deletion patterns [30], or the high-throughput chromosome capture (Hi-C) method should be used to understand the effect of 3D genome architecture on gene expression after radiation exposure.

In summary, the delayed response to radiation exposure is described in terms of gene expression in the progeny of survivors exposed to X-rays. The large deletion around the *HPRT1* locus influences on other gene expressions through up- or down-regulation of the entire X chromosome, and this effect persists in the progeny specifically. This suggests that chromosomal structure not only around the *HPRT1*-deletion site, but also distant from the *HPRT1* locus are involved in whole-genome gene expression in progeny cells. The data provide new avenues for understanding radiation-induced genomic instability by suggesting the existence of cell-specific gene regulation in the progeny cells as a "radiation signature".

CHAPTER 3: Metabolic effects

3.1 Introduction

Radiotherapy is one of the principal cancer treatments, and radiation exposure has been shown to elicit irreversible gap 1 (G1)-arrest and early senescence in normal human cells [1-3]. Previous studies have demonstrated radiation therapeutically-induced senescence [4,5], in which both cancer cells and normal stromal cells irreversibly arrest at the G1 phase and exhibit senescent phenotypes [6-8]. Senescent stromal and cancer cells can alter the tissue microenvironment through inflammatory responses of cells in exposed organs and may be implicated in the development of secondary carcinogenesis.

X-ray stress, as a typical ionizing radiation form induces the expression of p21, which functions downstream of the p53 pathway and suppresses the cyclin-dependent kinase 2 (CDK2) complex pathway [9]. p16 also inhibits the cyclin-dependent kinases 4 and 6 (CDK4/6) complex [10]. Inhibitions of these cyclin-CDK pathways leads to irreversible cell-cycle arrest, as these cyclin-CDK complexes activate the transcription factor E2F, which is essential for cell cycle progression [11]. More recently, a complex process rather than a simple one has been considered as the regulator of irreversible cell-cycle arrest [4,5,12,13].

Mitochondria also decrease mitochondrial function in irreversible cell-cycle arrest by increasing the production of reactive oxygen species (ROS) induced by X-rays [14,15]. ROS open the mitochondrial permeability transition pore, decrease the nicotinamide adenine dinucleotide/ nicotinamide adenine dinucleotide and hydrogen (NAD^+ /NADH) ratio [16], activate adenosine monophosphate (AMP)-activated protein kinase, and increase p53 expression by AMP-activated protein kinase, resulting in p21 expression [17-19]. CDK inhibitors induce expression of other downstream genes, a process that may reduce mitochondrial function and induce irreversible cell-cycle arrest. Therefore, for a comprehensive understanding of the biological effect of irreversible cell-cycle arrest, it is essential to clarify mitochondrial energy metabolism during the progression of irreversible cell-cycle arrest. It was previously reported that the total mitochondrial area increases in hypertrophied cells (i.e., irreversible cell-cycle-arrested cells). Hypertrophy occurs when cells evade entry into mitosis to form tetraploid cells and this leads to the increase in mitochondria that accompanies the increase in cell size [20]. Since eukaryotic cells attempt to maintain optimal size to maintain homeostasis, and cell contents such as mitochondria are linearly proportional to cell size, adenosine triphosphate (ATP) production is also expected to increase in hypertrophied senescent cells. However, cells undergoing irreversible cell-cycle arrest are assumed to require less ATP than normal cells because 60% of the total energy production by aerobic metabolism is utilized per cell cycle [21], which requires validation in radiation-induced irreversible cell cycle arrest.

In this study, mitochondrial content was examined by mitotracker green (MTG) staining and mitochondrial membrane potential ($\Delta\Psi m$) through 5,5′,6,6′-tetraethyl-benzimidazolylcarbocyanine iodide (JC-1) staining to ascertain the irreversible cell-cycle arrest induced by X-irradiation. The irreversible cell-cycle arrest induced by X-irradiation was characterized. Since ionizing radiation prompts early irreversible cell-cycle arrest in stromal cells [22,23], specifically fibroblasts, WI-38 cells ware irradiated with 20 Gy X-rays to examine the effects of irradiation on fibroblasts. The irreversible cell-cycle arrest induced by radiation alone was also examined using immortalized BJ-5ta cells, which do not display endogenous senescence due to telomere shortening.

3.2 Materials and methods

3.2.1 Cell lines and culture conditions

Primary human fetal lung fibroblasts (WI-38 from the American Type Culture Collection, Virginia, USA) and human TERT-immortalized foreskin fibroblast-like cells (BJ-5ta from the American Type Culture Collection, Virginia, USA) were used (Figure 3-1). WI-38 cells were cultured in D-MEM medium (Fujifilm Wako Pure Chemical Industries, Osaka, Japan) supplemented with L-glutamine and phenol red, 10% fetal bovine serum (Thermo Fisher Scientific, Massachusetts, USA), and 1% antibiotic-antimycotic (Thermo Fisher Scientific, Massachusetts, USA). BJ-5ta cells were grown in a medium consisting of a 4:1 ratio of D-MEM (Fujifilm, Tokyo, Japan) and Medium 199 (Sigma-Aldrich, St. Louis, MO) with the addition of 10% fetal bovine serum (Thermo Fisher Scientific, Massachusetts, USA) and 1% antibiotic-antimycotic (Thermo Fisher Scientific, Massachusetts, USA). Cells were incubated at 37°C in a humidity-controlled environment with a gas composition of 95% air and 5% CO_2.

Experiments were independently repeated three times, with cells seeded two days prior to irradiation. For cell proliferation measurements, 2.0×10^5 cells/well were seeded on Falcon T25 flasks (Corning, New York, USA). For 5-ethynyl-2′-deoxyuridine (EdU) staining, 2.0×10^4 cells/well were seeded on Falcon plastic 96-well plates (Corning, New York, USA). Senescence-associated β-galactosidase (SA-β-gal) staining was performed with 5.0×10^4 cells/well seeded on Falcon plastic 35-mm cell culture dishes (Corning, New York, USA), and MTG and JC-1 staining was performed with 5.0×10^4 cells/well seeded on glass 35-mm cell culture dishes (Iwaki, Tokyo, Japan). Before irradiation, the growth medium was replenished with fresh medium, and the cells were incubated without changing the medium.

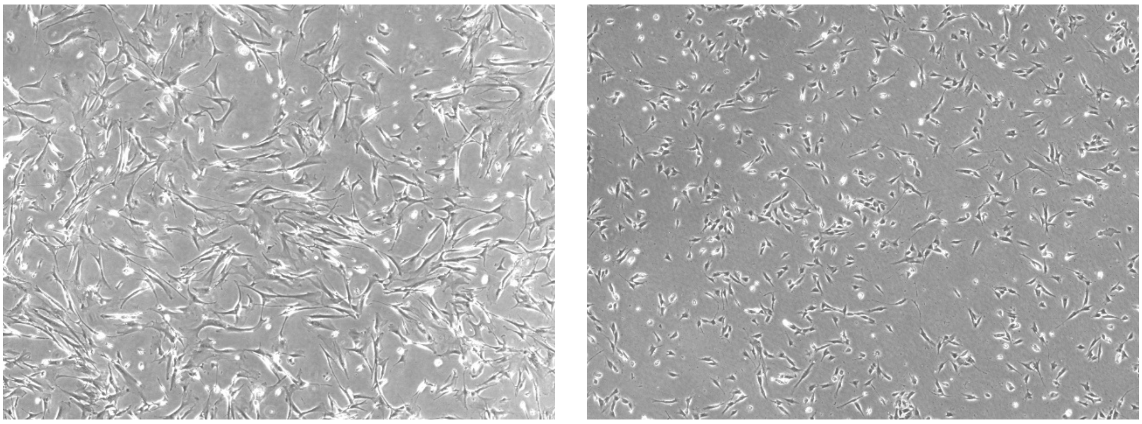

WI-38 BJ-5ta

Figure 3-1. Microscopic images of WI-38 and BJ-5ta cells on a dish.

Primary WI-38 cells and hTERT-immortalized BJ-5ta cells are shown in the phase contrast microscopic images.

3.2.2 X-ray irradiation

The cells were exposed to X-rays using an X-ray generator equipped with a tungsten target (M-150WE; Softex, Tokyo, Japan). The energy spectrum of the characteristic X-rays was between 60-70 keV. A 0.2-mm-thick aluminum filter was used to attenuate the presence of low-energy X-rays (< 1.5 keV). The X-ray generator was operated at a tube voltage of 150 kVp and a tube current of 3.48 mA, resulting in a dose rate of 1.0 Gy/min. The cells were exposed to X-rays for 20 minutes, resulting in a total dose of 20 Gy.

3.2.3 Live-cell imaging using microscope

Cell samples were examined under a BZ-710X fluorescence microscope (Keyence, Osaka, Japan) (Figure 3-2). The excitation and emission wavelengths used for 4′,6-diamidino-2-phenylindole (DAPI) were 360 and 460 nm, respectively, while those used for MTG were 490 and 516 nm. For JC-1, the excitation and emission wavelengths were either 485 and 535 nm (for green fluorescence) or 520-570 and 570-610 nm (for red fluorescence), respectively. Filters specifically designed to absorb light (Keyence) for DAPI (460 ± 50 nm), green fluorescent protein (525 ± 50 nm), and tetramethylrhodamine-5-(and -6-) isothiocyanate (605 ± 70 nm) were used to obtain green, red, and blue fluorescence. Phase contrast images were taken in addition to fluorescence observations. Cell samples were maintained in a temperature-controlled, humidified chamber (Tokai Hit, Shizuoka, Japan) at 37°C and 5% CO_2 inside the fluorescence microscope. The 20× magnification objective for EdU, 10× magnification for SA-β-gal, or a 60× oil immersion objective for MTG and JC-1 were adjusted and equilibrated for approximately 30 min before observations to ensure consistent temperature conditions. Observations were performed using the BZ-X Viewer microscope control application software (Keyence, Osaka, Japan).

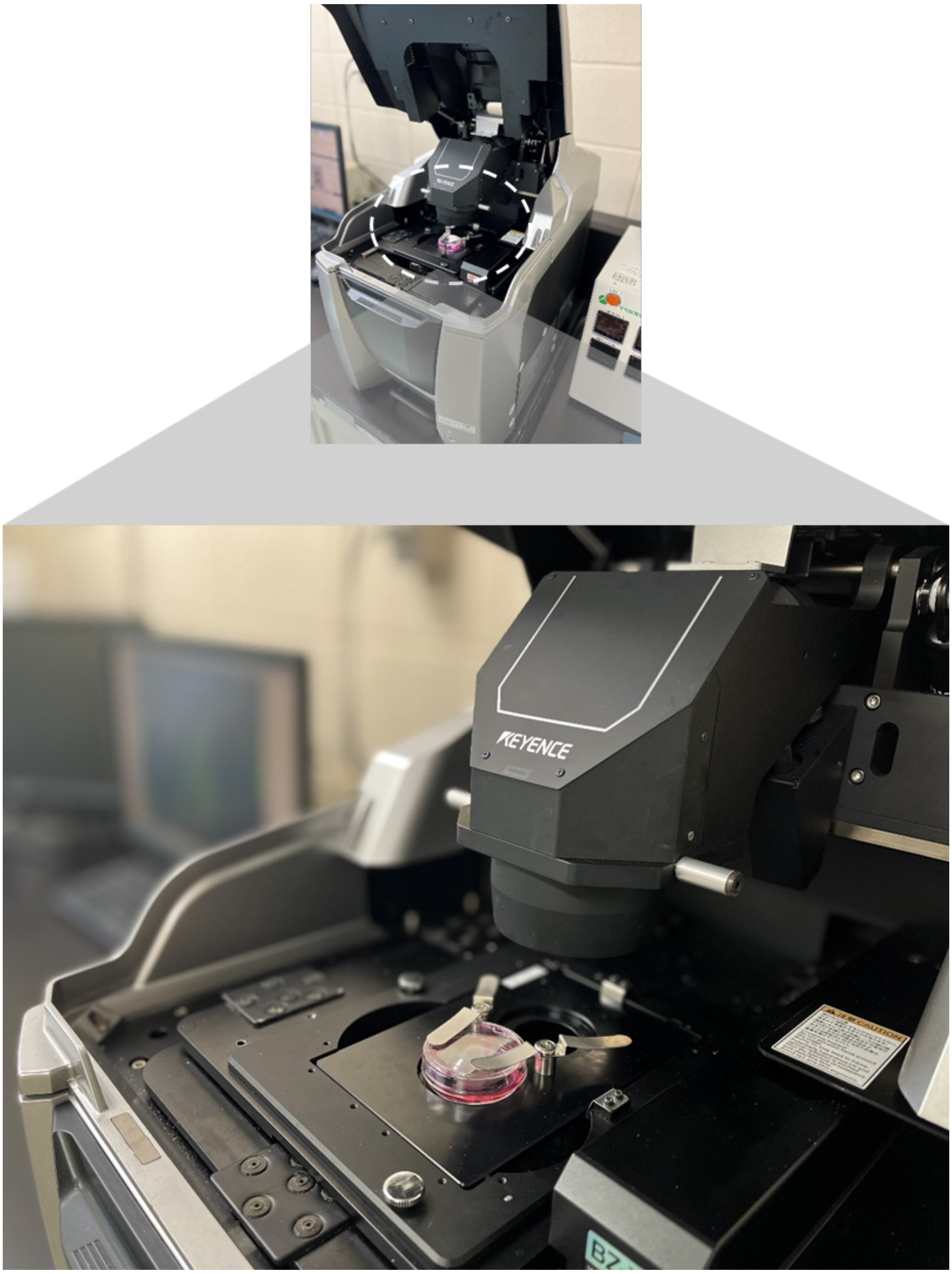

Figure 3-2. Photographs of the sample set in the fluorescence microscope.

The cell sample in a 35 mm dish was placed in the BZ-710X fluorescence microscope.

3.2.4 Measurement of cell proliferation

Non-irradiated and X-irradiated WI-38 and BJ-5ta cells exposed to a dose of 20 Gy were maintained in an incubator for 9 and 15 days, respectively. The cells were rinsed with PBS and then treated with 0.05% trypsin-EDTA (Thermo Fisher Scientific, Tokyo, Japan) for 3 min in the incubator. The cells were then resuspended in serum supplemented medium to inactivate trypsin. Cell counting was performed using a Coulter counter (Beckman Coulter, California, USA). BJ-5ta cells were cultured for a longer period of time compared to WI-38 cells because they are an immortalized cell line derived from human telomerase reverse transcriptase (hTERT), which may result in molecular variations compared to primary cells such as WI-38.

3.2.5 EdU staining

5-ethynyl-2′-deoxyuridine (EdU) is an alternative to 5-bromodeoxyuridine and represents a thymidine analogue. Detection and quantification of cell proliferation was performed using an EdU proliferation kit (Abcam, Cambridge, UK). Cells were incubated for 2 h in an incubator containing the EdU solution. Cells were then incubated for a further 15 min at room temperature with a fixative solution added to each well. During this time, the culture plate was maintained in a protected, light-free environment. Cells were washed twice with wash buffer before storage in PBS in an incubator to prevent desiccation. After the cells from all of the conditions had been fixed, they were stained on the same day. A permeabilization buffer was added to the cells and they were incubated for 20 min at room temperature. After two washes with the wash buffer, a reaction mix was added to the cells for staining and the cells were incubated for 30 min at room temperature. The cells were washed again with the wash buffer and PBS, and the nuclei were labeled with DAPI (Dojindo, Kumamoto, Japan). Finally, fresh PBS was added for microscopic observation of EdU-positive cells.

3.2.6 SA-β-gal staining

SA-β-gal staining is used to differentiate irreversible cell cycle arrest [25]. A Senescence Cells Histochemical Staining Kit (Sigma-Aldrich, Missouri, USA) was used for SA-β-gal staining. Cells were washed twice with PBS, fixed with fixation buffer, and incubated at room temperature for 7 min. The cells were then rinsed three times with PBS and stored in a PBS solution at 4°C, with the dishes covered with parafilm to prevent desiccation. Cells in all conditions were then fixed under the cover of parafilm to prevent exposure to atmospheric CO_2, which can lower the pH level of the buffer and affect staining efficiency. They were fixed and stained on the same day. The cells were incubated overnight and washed three times with PBS. The cells were then examined microscopically. The percentage of SA-β-gal-positive cells was determined by plotting the number of positive cells (blue) against the total number of cells in each field of view.

3.2.7 Mitochondria staining

The mitochondrial area was analyzed using the chemical probe MTG (purchased from Invitrogen, Massachusetts, USA). The MTG probe labels mitochondria with a green-fluorescent signal independent of the $\Delta\Psi m$ value. The MTG probe was diluted with dimethyl sulfoxide (DMSO) to a stock concentration of 100 μM and stored at 20°C prior to use. The stock solution was equilibrated to room temperature and mixed with D-MEM to a final concentration of 200 nM, which served as the staining solution. The D-MEM medium was removed from the glass dish containing the cultured cells and the staining solution was added. After 20 min of incubation in a cell incubator, the solution was removed from the dish and the cells were washed twice with PBS. Fresh D-MEM medium was added for subsequent observation under a fluorescence microscope.

3.2.8 ATP detection

A commercial Intercellular ATP measurement kit (IC2-100, TOYO B-Net, Tokyo, Japan) was used to extract ATP and measure the amount of ATP by the luciferin-luciferase method. A luciferase enzyme oxidizes luciferin substrate by using ATP, O_2, and Mg^{2+}. This chemical reaction results in the formation of the excited state oxyluciferin, which emits visible light upon transition to the ground state as shown in the formula below. Since the intensity of the emitted light is proportional to the amount of ATP, the light was measured as the amount of ATP.

$$Luciferin + ATP + O_2 \xrightarrow{luciferase, Mg^{2+}} oxyluciferin + AMP + PPi + CO_2 + light$$

To prepare the ATP light-emitting reagent, the ATP light-emitting reagent (lyophilized) and the dissolver were thawed at room temperature. The entire contents of one bottle (12 ml) of the dissolver was added to the vial containing the ATP light-emitting reagent and the vial was slowly inverted several times to mix thoroughly. The vial was allowed to stand at room temperature for an hour to acclimate the reagent. The ATP emitting reagent and the ATP standard reagent were dispensed and stored at −80 °C prior to use, to avoid affected by light, temperature, or physical stimuli.

The medium was removed from the 96-well plate of cell samples prepared two days earlier, and then the cells were washed with PBS and 100 µl of the ATP extraction solution was applied to each of the well. After gently shaking the plate for 5 min at room temperature, the reagent in each of the well was pipetted and collected in a tube placed on ice. Ten µl of the ATP extraction reagent was added to a measuring tube containing 100 µl of the prepared ATP light-emitting reagent. The reagent in a tube was gently shaken and measured with a luminometer (GL-200, Microtec Nichion, Chiba, Japan).

3.2.9 Detection of mitochondrial membrane potential

The ΔΨm was visualized using the JC-1 chemical probe obtained from a commercial kit (Cayman Chemical, Michigan, USA). This kit contains a monomer that fluoresces green at low ΔΨm (≤ −100 mV) and a polymer that fluoresces red at high ΔΨm (≥ −140 mV). The JC-1 reagent was thawed, equilibrated to room temperature, and then combined with 225 µL D-MEM to form a stock solution, which was stored at −20°C prior to use. To prepare a working solution, 25 µL of the stock solution was mixed with 500 µL of D-MEM. The D-MEM medium was removed from the glass culture dish, and the working solution was added to the cells and incubated for 20 min in a cell incubator. After the incubation period, the solution was removed from the dish and the cells were washed twice with PBS. Fresh D-MEM medium was added for observation under a fluorescence microscope.

3.3 Results

3.3.1 Cell proliferation against 20 Gy X-ray dose

In WI-38 cells, the expression of irreversible cell-cycle arrest was examined by enumerating the number of non-irradiated (0 Gy) and 20 Gy X-irradiated cells (Figure 3-3). Non-irradiated WI-38 cells showed a 10-fold increase in proliferation after up to 9 days of culture, whereas cell proliferation was significantly suppressed in 20 Gy X-irradiated WI-38 cells. Similarly, non-irradiated BJ-5ta cells exhibited a significant increase in proliferation after reaching confluence in culture for up to 7 days, but the proliferation of 20 Gy X-irradiated cells was significantly lower than that of non-irradiated cells.

In certain tumor cell lines, 20 Gy irradiation results in significant cell loss [25]. However, in WI-38 and BJ-5ta, no such diminution in cell number was observed after 20 Gy irradiation, and most cells (90%) persisted in culture without progressing through the cell cycle. This result is consistent with previous study [26] and confirms that 20 Gy of X rays induces irreversible cell-cycle arrest without cell loss. Therefore, 20 Gy is determined to be the appropriate dose to induce irreversible cell-cycle arrest.

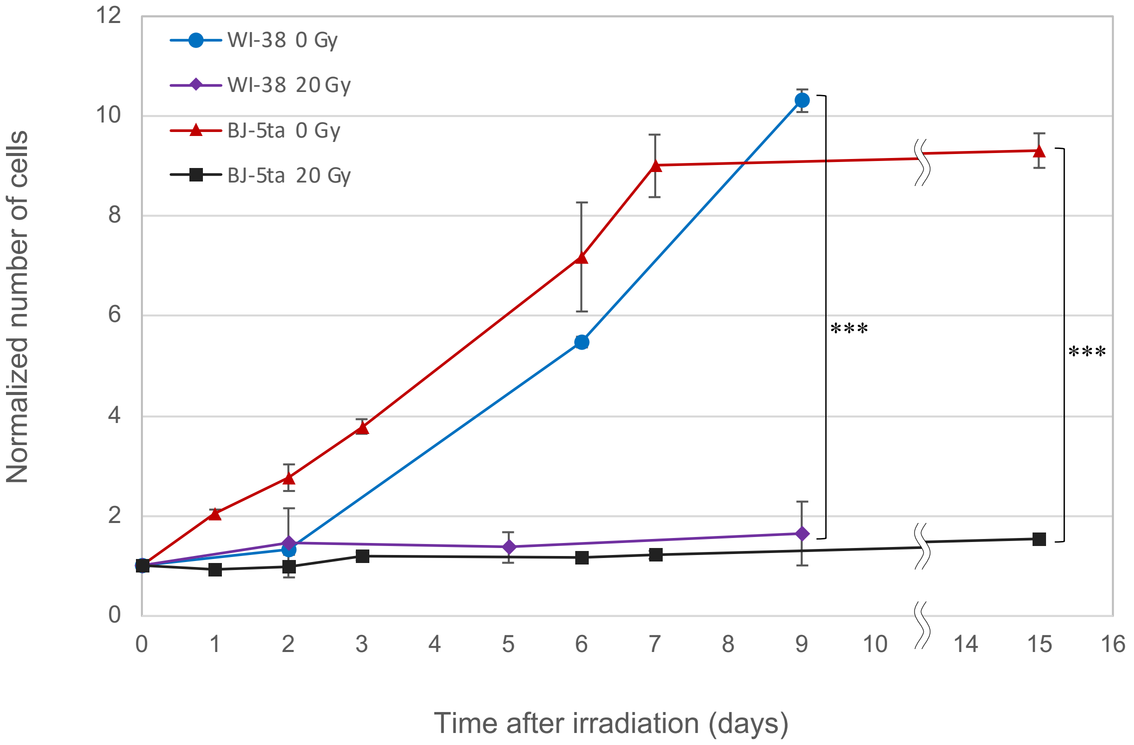

Figure 3-3. Effect of 20 Gy X-ray dose on WI-38 and BJ-5ta cell proliferation.

The number of non-irradiated and 20 Gy X-irradiated cells (seeded at 2.0×10^5 cells/well) was counted over a period of 9 days for WI-38 cells and 15 days for BJ-5ta cells. All values were normalized to the number of cells at day 0, and the error bars represent the standard deviation (SD) (n = 3). The symbol * indicates the p-values of the Student's t-test compared to the non-irradiated and irradiated samples, respectively; *** $p < 0.001$.

3.3.2 Cell-cycle arrest conformation by EdU- and SA-β-gal staining

The irreversible cell-cycle arrest of WI-38 cells after 20 Gy X-irradiation was confirmed by EdU-labeling experiments. Irreversible cell-cycle arrest induction was also verified by SA-β-gal staining [27]. As shown in Figure 3-4, the majority of cells after irradiation were negative for EdU staining; when the percentage of EdU-positive cells was plotted against time after irradiation (Figure 3-5), all values after irradiation were less than 2%. In contrast, SA-β-gal blue staining decreased in a time-dependent manner after irradiation (Figure 3-6). The percentage of SA-β-gal positive cells in three randomly selected microscopic fields of view increased in a time-dependent manner, reaching approximately 90% by 9 days after irradiation (Figure 3-7). BJ-5ta cells also showed a similar trend as WI-38 cells. These results confirm that 20 Gy X-irradiation induces irreversible cell-cycle arrest, often referred to as premature senescence

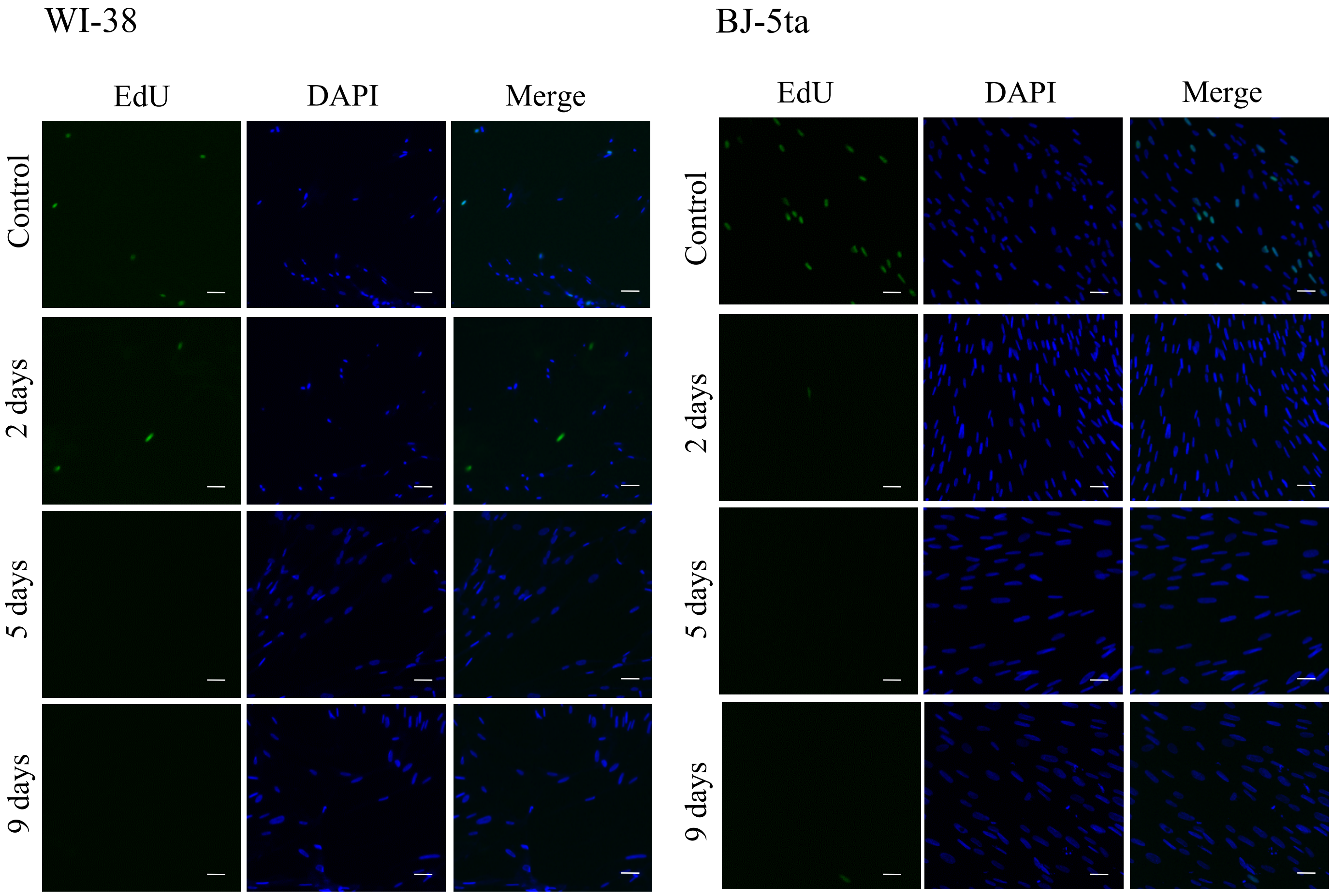

Figure 3-4. Representative microscopic images of EdU- and DAPI-stained non-irradiated (control) and irradiated WI-38 and BJ-5ta cells.

Non-irradiated (control) and 20 Gy X-irradiated WI-38 and BJ-5ta cells were stained with EdU and DAPI and then observed under a fluorescence microscope at 20× magnification. Images of the irradiated cells were taken at 2, 5, and 9 days after irradiation. EdU (green) was added for 2 h before analysis. Cells were counterstained with DAPI (blue). The scale bar is 50 µm for all images.

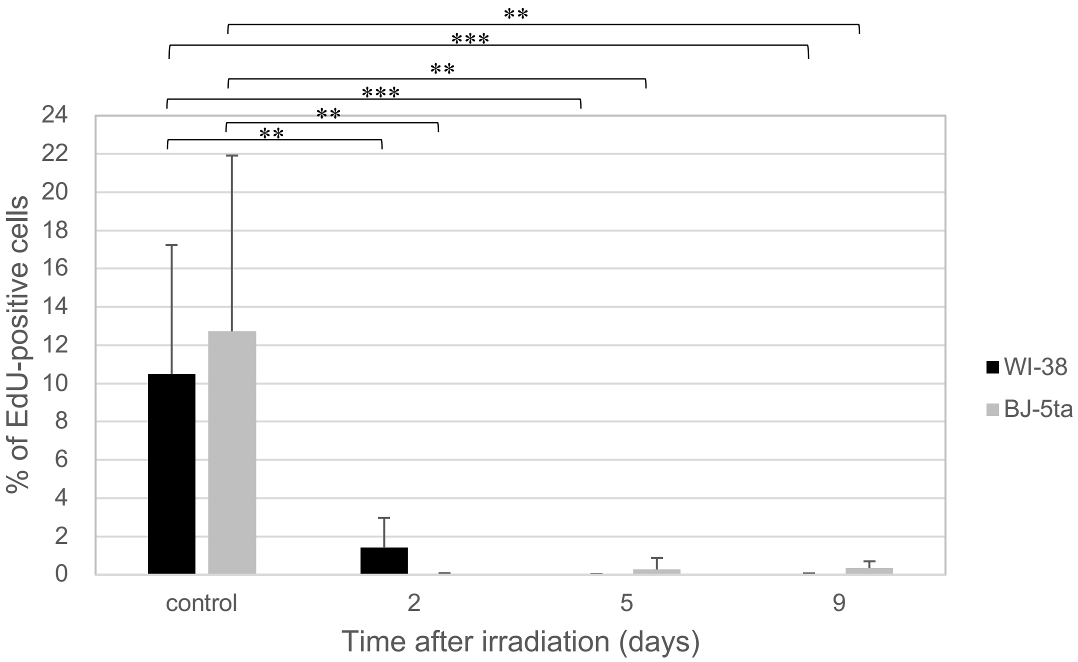

Figure 3-5. Percentage of EdU-positive cells in non-irradiated (control) and irradiated WI-38 and BJ-5ta cells.

The percentages of EdU-positive non-irradiated (control) and 20 Gy X-irradiated WI-38 and BJ-5ta cells were obtained from EdU staining and DAPI counterstaining. Data from the irradiated cells were obtained at 2, 5, and 9 days after irradiation. EdU-positive cells were divided by the total number of cells in each microscopic field, and the fraction was multiplied by 100. Approximately 200 cells were counted in each field. The error bars represent the standard deviation (SD) (n = 3). Statistical analysis was performed using Student's t-test. The symbol * indicates the p-value of the t-test compared with the control and irradiated samples, respectively; *** $p < 0.001$, ** $p < 0.01$.

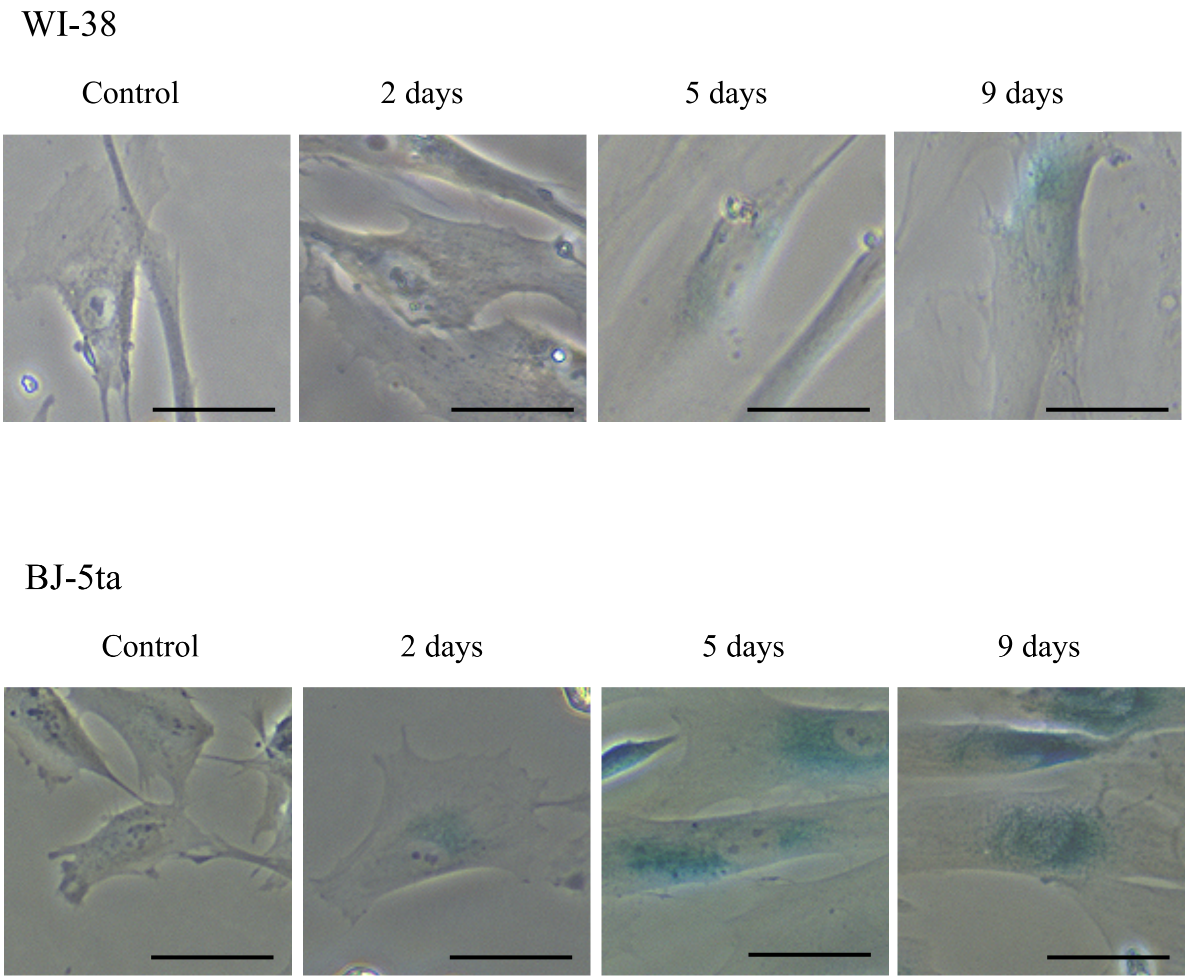

Figure 3-6. Representative microscopic images of SA-β-gal-stained non-irradiated (control) and irradiated WI-38 and BJ-5ta cells.

Non-irradiated (control) and 20 Gy X-irradiated WI-38 and BJ-5ta cells were stained with SA-β-gal and then observed under a fluorescence microscope at 20× magnification. Images of the irradiated cells were taken at 2, 5, and 9 days after irradiation. The blue color indicates the detection of SA-β-gal. the scale bar is 50 μm for all images.

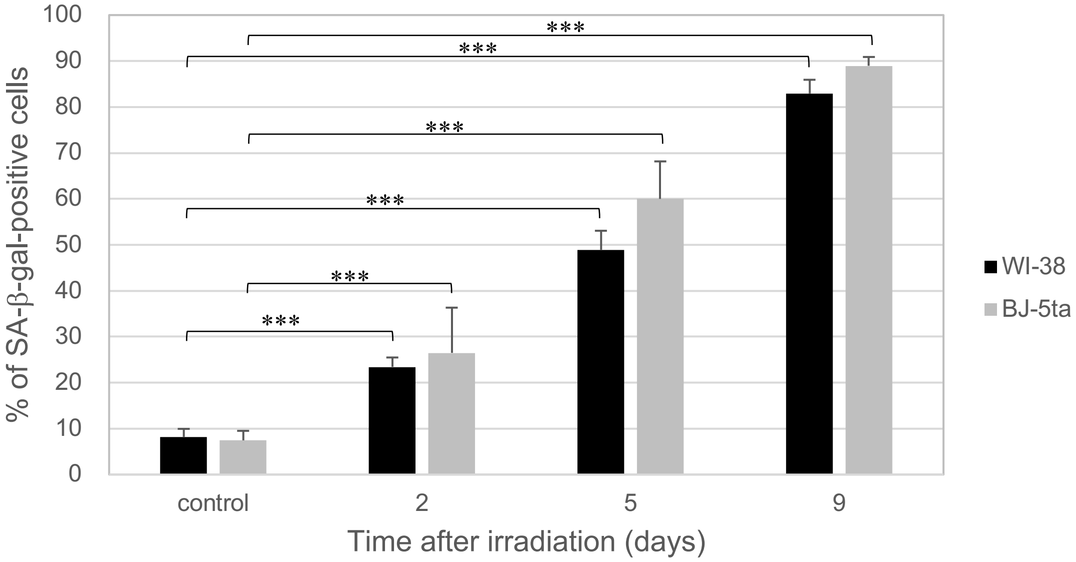

Figure 3-7. Percentage of SA-β-gal-positive cells in non-irradiated (control) and irradiated WI-38 and BJ-5ta cells.

The percentages of the SA-β-gal-positive non-irradiated (control) and 20 Gy X-irradiated WI-38 and BJ-5ta cells were obtained from SA-β-gal staining. Data from the irradiated cells were obtained at 2, 5, and 9 days after irradiation. SA-β-gal-positive cells were divided by the total number of cells in each microscopic field, and the fraction was multiplied by 100. Approximately 70 cells were counted in each field. The error bars represent the standard deviation (SD) ($n = 3$). Statistical analysis was performed using Student's t-test. The symbol * indicates the p-value of the t-test compared with the control and irradiated samples, respectively; *** $p < 0.001$.

3.3.3 Mitochondrial and cellular area changes over time after irradiation

Analysis of MTG-stained mitochondria showed an increase in total mitochondrial area and persistent hypertrophic changes in cell morphology after exposure (Figure 3-8). Mean total mitochondrial area per cell (Figure 3-9) and mean cell area determined by phase-contrast imaging (Figure 3-10) were plotted against time after exposure. There was a continuous increase in total mitochondrial area and cellular area over time in WI-38 and BJ-5ta cells. The ratio of mitochondrial area to cell area (Table 3-1), calculated as mean total mitochondrial area divided by mean cell area, showed a decrease in WI-38 cells after irradiation, but no significant decrease in BJ-5ta cells.

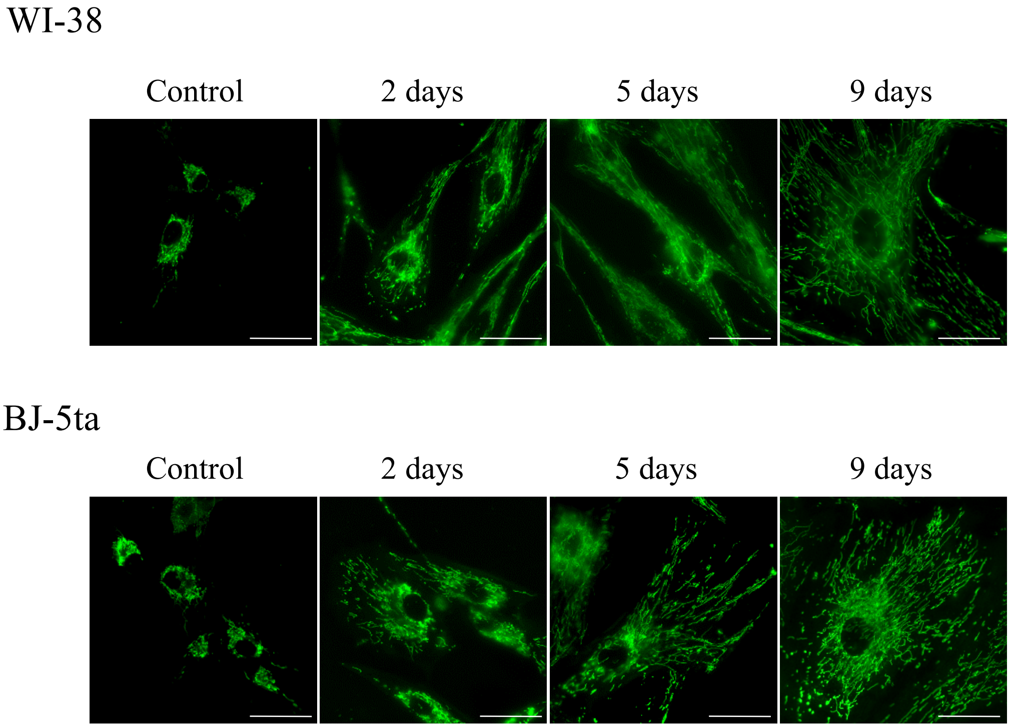

Figure 3-8. Representative microscopic images of MTG-stained mitochondria from non-irradiated (control) and irradiated WI-38 and BJ-5ta cells.

Non-irradiated (control) and 20 Gy X-irradiated WI-38 and BJ-5ta cells were stained with MTG and then observed under a fluorescence microscope at 60× magnification. Images of the irradiated cells were taken at 2, 5, and 9 days after irradiation. The scale bar is 50 µm for all images.

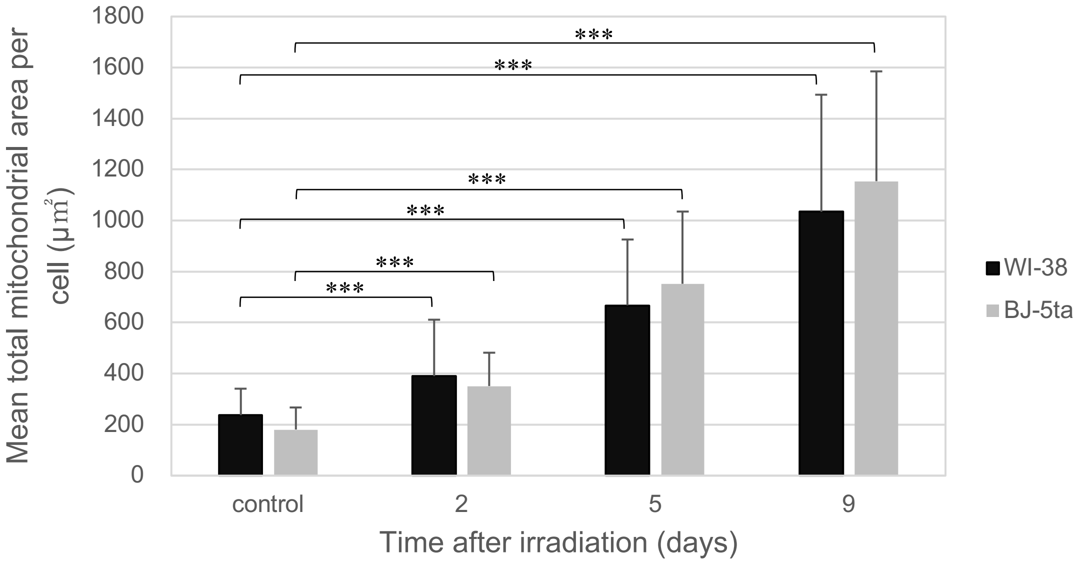

Figure 3-9. Mean mitochondrial area in non-irradiated (control) and irradiated WI-38 and BJ-5ta cells.

The mean total mitochondrial area in non-irradiated (control) and 20 Gy X-irradiated WI-38 and BJ-5ta cells were obtained from MTG staining. Data from the irradiated cells were obtained at 2, 5, and 9 days after irradiation. The error bars represent the standard deviation (SD) (n = 90). Statistical analysis was performed using Student's t-test. The symbol * indicates the p-value of the t-test compared with the control and irradiated samples, respectively; *** $p < 0.001$.

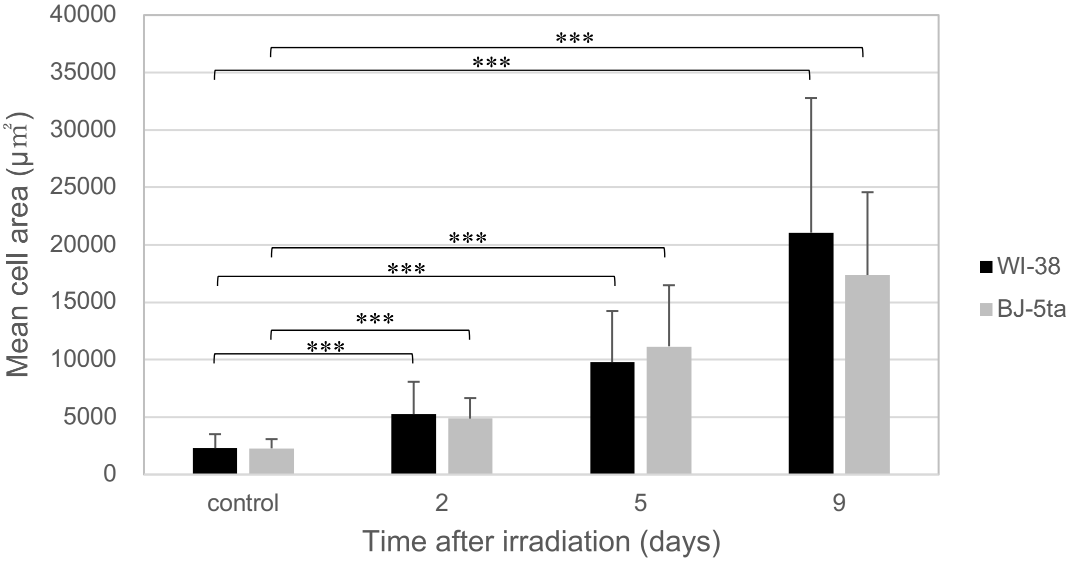

Figure 3-10. Mean cell area in non-irradiated (control) and irradiated WI-38 and BJ-5ta cells.

The mean total cell area of non-irradiated (control) and 20 Gy X-irradiated WI-38 and BJ-5ta cells were obtained from phase contrast images. Data from the irradiated cells were obtained at 2, 5, and 9 days after irradiation. The error bars represent the standard deviation (SD) (n = 90). Statistical analysis was performed using Student's t-test. The symbol * indicates the p-value of the t-test compared with the control and irradiated samples, respectively; *** $p < 0.001$.

Table 3-1. Geometry of the mitochondrial and cellular areas in non-irradiated (control) and irradiated WI-38 and BJ-5ta cells.

The total mitochondrial area was obtained by MTG staining. The cell area was obtained from phase contrast images.

	WI-38				BJ-5ta			
Time after irradiation (days)	Control	2	5	9	Control	2	5	9
Total mitochondrial area (μm^2)	237 (± 104)	390 (± 221)	668 (± 258)	1034 (± 459)	181 (± 86)	351 (± 131)	752 (± 283)	1155 (± 431)
Cell area (μm^2)	2290 (± 1220)	5270 (± 2810)	9770 (± 4470)	21,100 (± 11,700)	2280 (± 809)	4870 (± 1790)	11,200 (± 5320)	17,400 (± 7220)
Ratio (Total mitochondrial area / cell area)	0.10	0.074	0.068	0.049	0.079	0.072	0.067	0.067

The ratio represents the mean total mitochondrial area per unit cell area. The errors of plus or minus represent the standard deviation (SD) (n = 90).

3.3.4 ATP level changes over time after irradiation

Analysis of the quantified ATP levels showed a sustained increase in ATP levels in both WI-38 and BJ-5ta cells in correlation with time after irradiation (Figure 3-11). In WI-38 cells, ATP levels increased rapidly 2 days after irradiation and continued to increase gradually thereafter. By 9 days after irradiation, the ATP level was approximately 5-fold higher than that of the control. In BJ-5ta cells, the rate of increase was not as pronounced as in WI-38 cells, but with a slight decrease from 5 to 9 days after irradiation, it generally tended to increase during the experimental period, and the amount of ATP was approximately 2-fold that of the control at 9 days after irradiation.

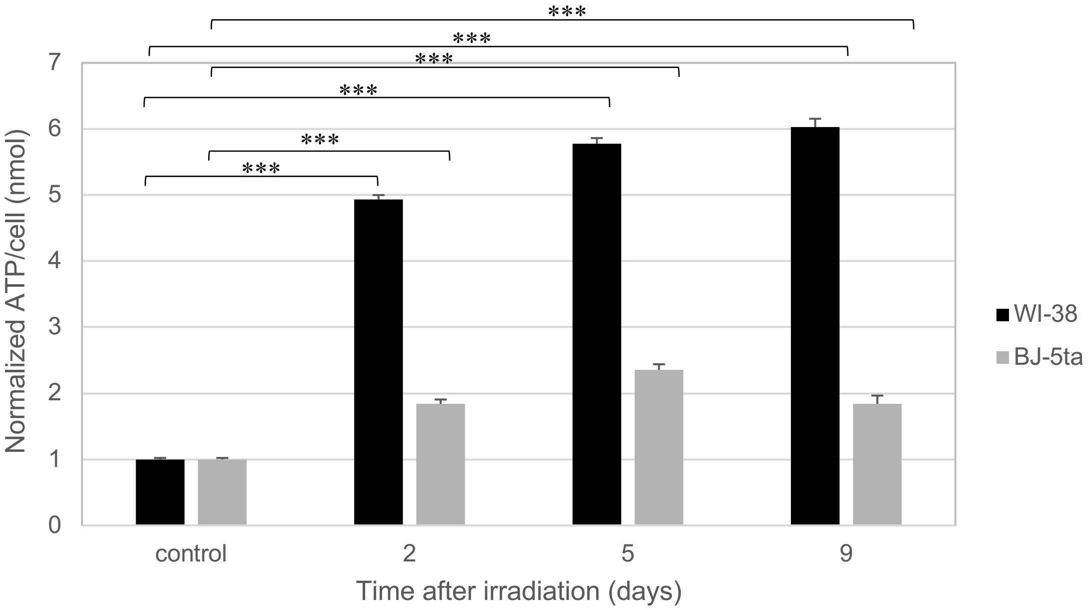

Figure 3-11. Normalized ATP amount of non-irradiated (control) and irradiated WI-38 and BJ-5ta cells.

ATP amount in non-irradiated (control) and 20 Gy X-irradiated WI-38 and BJ-5ta cells were estimated by the luciferin-luciferase method. Data from the irradiated cells were obtained at 2, 5, and 9 days after irradiation, and all values were normalized to the control cells. The error bars represent the standard deviation (SD) ($n = 3$). Statistical analysis was performed using Student's t-test. The symbol * indicates the p-value of the t-test compared with the control and irradiated samples, respectively; *** $p < 0.001$.

3.3.5 Mitochondrial membrane potential changes over time after irradiation

The area of low mitochondrial membrane potential (green) within each X-irradiated cell line enlarged as the cellular morphology expanded. Conversely, the area of high mitochondrial membrane potential (red) did not show a time-dependent increase after irradiation (Figure 3-12). The fraction of high mitochondrial membrane potential area within the total JC-1 staining area was normalized to the fraction of the control cells and plotted against time after irradiation (Figure 3-13). In WI-38 cells, a minimum value of the fraction was observed on the second day after irradiation and then increased rapidly (1.8-fold the control value). In contrast, in BJ-5ta cells, a slight minimum value was observed on the second day after irradiation, followed by a gradual increase, but it did not exceed the control value.

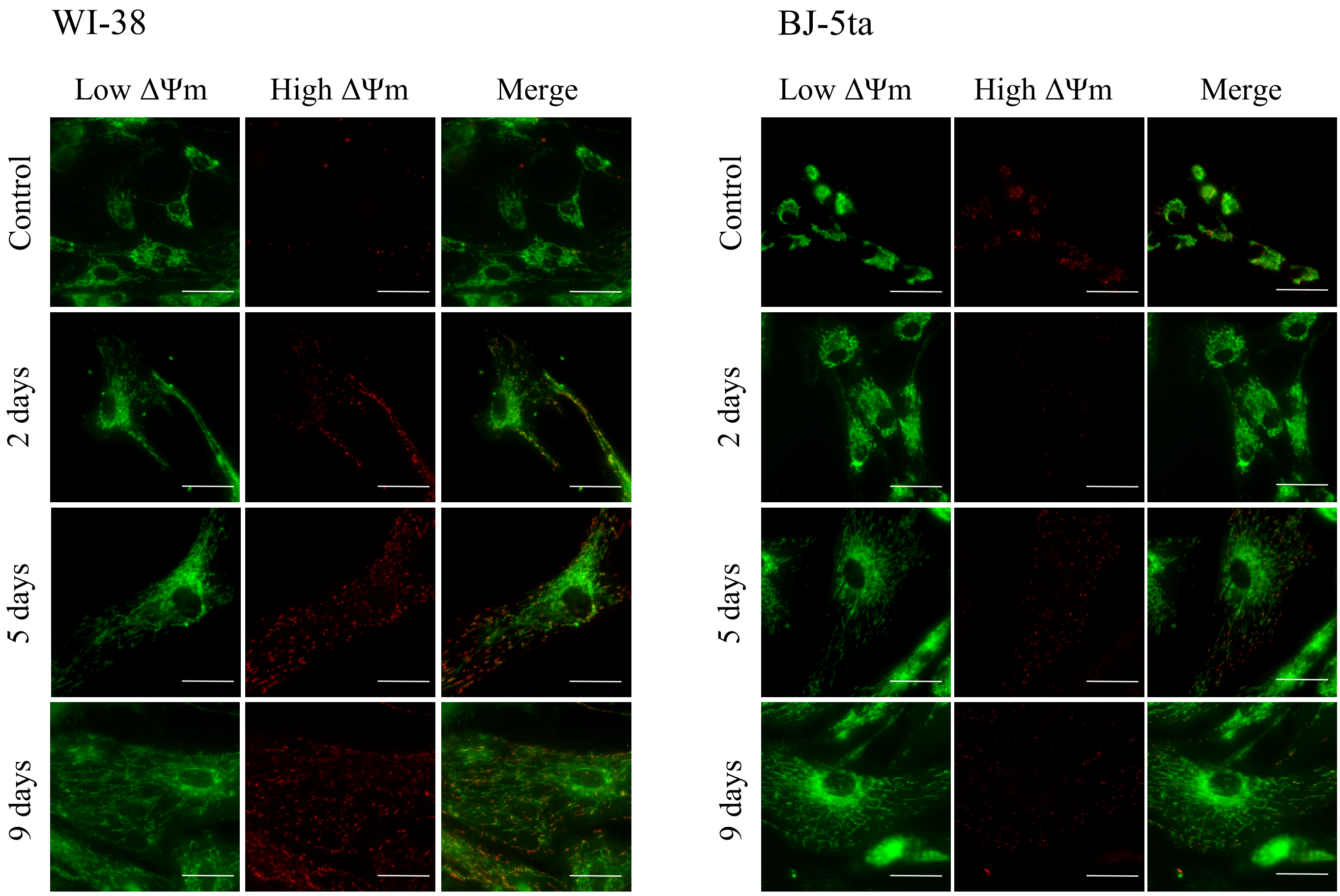

Figure 3-12. Representative images of the low and high ΔΨm regions with JC-1 staining of non-irradiated (control) and 20 Gy X-irradiated WI-38 and BJ-5ta cells.

Non-irradiated (control) and 20 Gy X-irradiated WI-38 and BJ-5ta cells were stained with JC-1 and then observed under a fluorescence microscope at 60× magnification. Images of irradiated cells were taken at 2, 5, and 9 days after irradiation. The scale bar is 50 μm for all images.

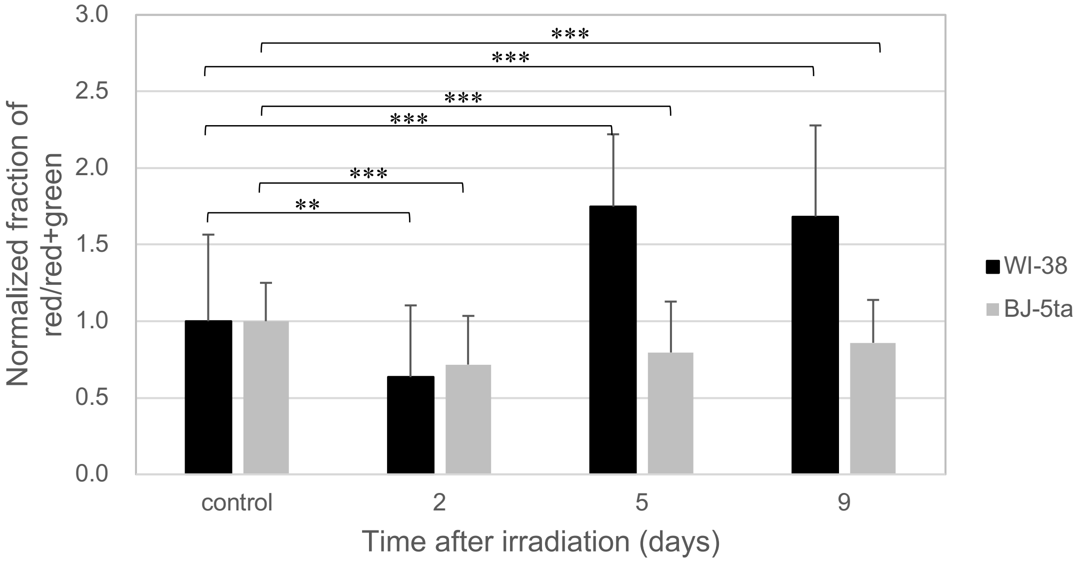

Figure 3-13. Normalized fraction of the high ΔΨm area defined as the ratio of the red areas to the sum of the red and green areas in non-irradiated (control) and irradiated WI-38 and BJ-5ta cells.

The red/red+green fluorescence ratios of JC-1 in non-irradiated (control) and 20 Gy X-irradiated WI-38 and BJ-5ta cells are shown. Data from the irradiated cells were obtained at 2, 5, and 9 days after irradiation, and all values were normalized to the control cells. The error bars represent the standard deviation (SD) (n = 90). Statistical analysis was performed using Student's t-test. The symbol * indicates the p-value of the t-test compared with the control and irradiated samples, respectively; *** $p < 0.001$, ** $p < 0.01$.

3.4 Discussion

The irreversibly cell-cycle arrested cells used in this study share many similarities with senescent cells [28], such as permanent loss of proliferative capacity as evidenced by EdU staining (Figure 3-5), enlarged cell size, flattened morphology (Figure 3-6), and expression of SA-β-gal (Figure 3-7), and it was confirmed that WI-38 and BJ-5ta cells induce senescence through irreversible cell-cycle arrest. Thus, WI-38 and BJ-5ta cells, the representative fibroblast cell lines used in this study, could induce premature senescence and maintaining metabolism without apoptotic features even after high-dose X-irradiation (20 Gy) (Figure 3-3). Whether the irreversible cell-cycle arrest is a general feature of X-irradiated normal cells remains to be clarified by using different normal cells of different tissue origin, but it has been confirmed that WI-38 cells and BJ-5ta cells enter a state of irreversible cell-cycle arrest.

This study is the first to report on changes in mitochondrial metabolism in cells undergoing irreversible cell-cycle arrest. Many studies on the radiation effects of irreversible cell-cycle arrested cells on mitochondria have reported functional impairment as revealed by fragmentation, reactive oxygen species (ROS) production, ATP concentration, and mitochondrial gene expression (see [29] and references therein for a review). However, little is known about mitochondria in cells with irreversible cell-cycle arrest; the increase in total mitochondrial area stained with MTG in WI-38 and BJ-5ta cells up to 9 days after irradiation suggests that the production of mitochondria exceeds the removal of damaged mitochondria (Figure 3-9), possibly due to the autophagy process. In addition to the increase in mitochondrial area, both cells also showed an increase in cellular area (Figure 3-10), presumably due to the reproduction of cellular components without undergoing cell division (enlargement effect). The ratio of total mitochondrial area divided by cell area in both cells (Table 3-1) decreased continuously, particularly in WI-38 cells, reaching about half of the control at 9 days after irradiation, suggesting that the reproducing mitochondria were less vibrant than those of other cellular components.

The quantified amount of ATP tended to increase continuously in both WI-38 and BJ-5ta up to 9 days after irradiation (Figure 3-11). The reason for the increase in intracellular ATP content is thought to be due to increased ATP production resulting from increased ATP demand within the cells. However, it remains speculative whether the increase in ATP in senescent cells is due to increased ATP production or decreased ATP consumption. Therefore, the mitochondrial membrane potential ($\Delta\Psi m$) was quantified using JC-1 to reflect ATP production in the cell.

The normalized fraction of high $\Delta\Psi m$ area in WI-38 and BJ-5ta cells visualized by JC-1 staining reached its lowest level 2 days after irradiation (Figure 3-13). This suggests that mitochondrial activity was temporarily reduced due to the degradation of damaged mitochondria as reported earlier (as described above), followed by the re-establishment of the high $\Delta\Psi m$ area within a few days. The high $\Delta\Psi m$ area overshot in primary cells (WI-38) at 5 days after irradiation, but the immortalized BJ-5ta cells retained a fraction. A low fraction of high $\Delta\Psi m$ area was also reported in other immortalized human fibroblasts, BJ-1 h-TERT [30]. This suggests that upregulate of energy metabolism is delayed in primary cells, but not in immortalized cells. Conversely, the manipulation of immortalization may alter energy metabolism as it pertains to stress responses.

Since that less than 1% of mitochondrial proteins are encoded in the mitochondrial genome [31], nuclear DNA is responsible for the production of proteins or chaperones necessary for mitochondrial synthesis. To the best of our knowledge, the time required for full recovery of mitochondrial assembly has never been precisely measured. However, it is estimated to take at least one cell cycle, usually 16-24 hours, due to the need to assemble complex bilayer structures and various membrane protein complexes. Therefore, it is reasonable to assume that cells responded to the ATP demand by prioritizing the expansion of existing mitochondrial activation sites after rapidly decreasing the fraction of high ΔΨm area due to radiation exposure.

Interestingly, in WI-38 cells, the normalized fraction of high ΔΨm area increased markedly (1.8-fold over control values) at 5 and 9 days after irradiation (Figure 3-13). Since ΔΨm is formed by an electrochemical proton gradient for ATP synthesis [32,33], this marked increase in the fraction of high ΔΨm area may be due to the likely to be a response to the increased ATP demand at day 5 after irradiation. This is because it is now clear that cells with irreversibly cell-cycles arrested cells require more bioenergy [34]. This ATP requirement may be caused by senescence-associated heterochromatic foci (SAHF), cell-cycle arrest through activation of the p53-p21 and p16-Rb pathways, or mitotic evasion and transition to G1 phase. Furthermore, cells with irreversible cell-cycle arrest share many characteristics with senescent cells, most notably the synthesis of SASP-related proteins, which may be require ATP. Previous studies reported that 41% or 33% of genes in proliferating cells are upregulated or downregulated after irreversible cell-cycle arrest and downregulated or upregulated by the fact of mitochondrial depletion, respectively [35]. They found that the regulated genes included many SASP-related genes. In terms of gene regulation, it is suggested that mitochondria produce extra ATP for SASP and contribute to cellular homeostasis with irreversible cell-cycle arrest.

In immortalized BJ-5ta cells with manipulated telomeres and unrestricted cell division, variations over time after irradiation in relative mitochondrial area per cell area and the fraction of high ΔΨm area showed patterns comparable to WI-38, but the degree of increase or decrease in BJ-5ta cells was less than that observed in WI-38 cells. Cell line differences between WI-38 and BJ-5ta may explain the observed dissimilarity. Specifically, WI-38 cells are isolated from the lung tissue of a 3-month-old female embryo, whereas BJ-5ta is derived from the foreskin of a male patient. The discrepancy in response between cell lines may also be related to telomere function and mitochondria. Sahin et al. [36] discovered the existence of mitochondrial dysfunction in mice engineered to gradually lose telomere function. This was the outcome of reduced activity of PGC-1α and PGC-1β, key factors that regulate mitochondrial function. Decreased activity of these factors leads to a decrease in mitochondrial number and metabolic failure of the cell with irreversible arrest of the cell cycle. In other words, mitochondria in BJ-5ta cells may be less sensitive to X-irradiation. Immortalization of WI-38 cells may be necessary to determine the underlying cause of the discrepancy between the two cell lines' response to radiation. Furthermore, studies of fluorescently labeled mitochondria in cultured mammalian cells have shown that mitochondrial fission often results in the asymmetric generation of two daughter organelles, one with a high membrane potential and the other with a reduced membrane potential [37]. This underscores the need to study mitochondrial morphology to gain insight into the observed differences between the two cell lines.

Other additional studies are also necessary to clarify the precise correlation between mitochondrial action and maintenance of cellular function in irreversibly cell-cycle arrested cells. In particular, inhibiting ΔΨm with uncoupling agents such as carbonyl cyanide m-chlorophenyl hydrazone and using normal human lung fibroblasts (MRC5 and TIG-3) and ρ0 cells, which is cells without mitochondrial DNA [38], may be a useful approach. Furthermore, quantification of intracellular ATP production as an indicator of energy metabolism, and oxygen consumption rate and extracellular oxidation rate of living cells as indicators of mitochondrial respiration and glycolysis would clearly demonstrate the effect of X-irradiation on respiratory chain function.

In conclusion, the mitochondrial morphology of cells that have undergone irreversible cell-cycle arrest after high-dose X-irradiation have described. Their chronological morphology show increase in mitochondrial area in senescence-like cells, indicating that they became highly active to accommodate the increased ATP requirements of the cells. Unlike previously thought, irreversible cell-cycle arrested cells were not less vigorous, but were intensely active, suggesting that they may be affecting surrounding normal cells via high-energy metabolism. This study provides a window for understanding the role of long-lived cell-cycle arrested cells, or senescent cells, in organs and throughout the body.

CHAPTER 4: Conclusion and future perspective

Studies of genomic and metabolic effects as cellular responses to ionizing radiation are essential to elucidate the mechanism of long-term effects of radiation in organs or the whole body. These are the conclusions of this thesis. First, DNA deletions were widely distributed as a patchwork pattern reflecting the radiation track structure [1]. The evidence strongly suggests that clustered non-DSB type DNA damage, consisting of base lesions, SSBs, or AP sites that are closely located within one or two helical turns, may also induce delayed DSBs in the progeny cells of radiation surviving cells as well as those that are directly induced along the radiation tracks. These additional induced DSBs would cause genomic instability and alter gene expression due to their DNA shortening structures rather than those of normal cells [2]. Second, mitochondria in irreversible cell-cycle arrested cells were activated presumably due to the extra demand for ATP for SAHF, activation of the p53-p21 and p16-Rb pathways to arrest the cell cycle, or SASP [3]. This suggests that ROS, a byproduct of ATP, may attack organelles neighboring mitochondria and induce oxidative damage to them. These two studies suggest that delayed DSB and elevated radical levels in irreversible cell-cycle arrested cells may be factors in the induction of cancer, a typical long-term effect of radiation.

The findings provide new evidence that DNA damage can induce an extremely gradual progression of carcinogenesis on a timescale of years, in contrast to the molecular processes of ionizing radiation in the cell on a timescale of femto- to milli-seconds, even in cells that appear to be "quiescent" because the main DNA repair process has already been completed and cell division has begun, or that the cell-cycle has stopped and appears to be low risk of cancer since there is no DNA replication. The research showed that cells exposed to radiation have a tendency to affect surrounding cells not directly exposed to radiation, potentially leading to future oncogenesis. This is a long-term effect of radiation that could not be detected by observing cells immediately after exposure (Figure 4-1).

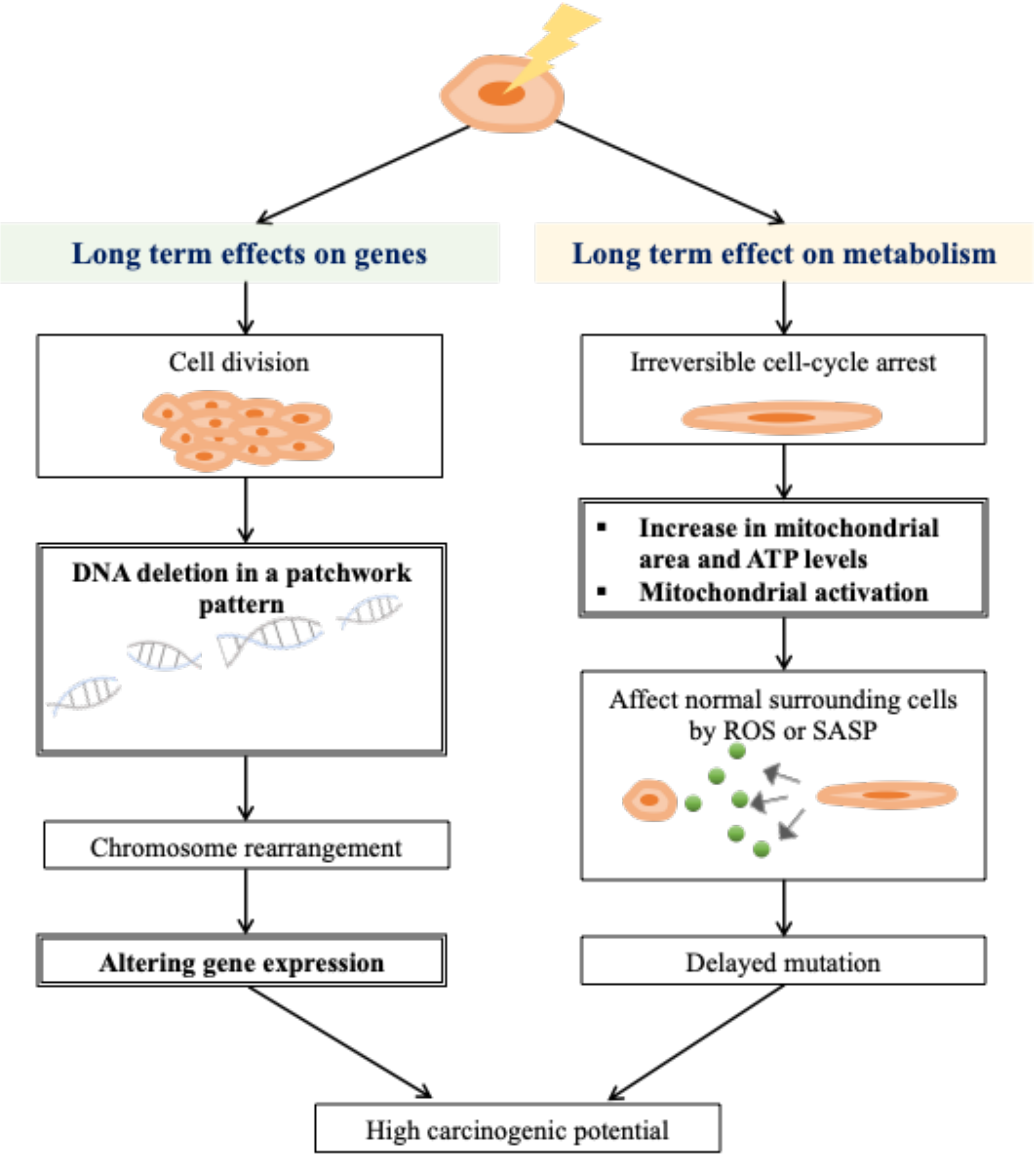

Figure 4-1. Summary of studies on long-term effects on genes and metabolism.
The double-lined boxes indicate new findings from this study. The study of the long-term effect of genes showed that even in the progeny of radiation surviving cells that are capable of cell division, there are DNA deletions in a patchwork pattern. Such deletions have the potential to induce chromosomal changes and shifts in altering gene expression. The study of the long-term effect on metabolism revealed an increase in both mitochondrial area and ATP levels, as well as mitochondrial activation in irreversible cell-cycle arrested cells. This suggests that ROS or SASP from irreversible cell-cycle arrested cells may damage normal surrounding cells and play a role in the development of delayed mutation. These cellular responses to radiation exposure may result in an increased carcinogenic potential.

The understanding of the risk of carcinogenesis from low-dose exposures of less than 100 mSv radiation is still chaotic. The International Commission on Radiological Protection (ICRP) has proposed the linear-no-threshold hypothesis (LNT hypothesis), which assumes that health effects are dose-dependent, no matter how small the exposure. However, there are many objections to whether the actual effects are linear or not, including the idea that DNA damage is repaired by DNA repair processes of cells in the low-dose range and thus the health risk is undetectable, and the opposite idea is that radiation-damaged cells can affect surrounding cells not exposed to radiation, leading to a greater risk of cancer in the low-dose range. The latter case is known as the "bystander effect", a typical nontargeted effect that occurs in distant cells [4]. My work in this thesis has focused on the temporal nontargeted effect arising from the progeny of radiation surviving cells, but this phenomenon has a similar mechanism to the latter case in terms of arising adverse impact on normal cells through the secretions of irreversible cell-cycle arrested cells. This study advances the understanding of the long-term biological effects of low-dose radiation.

There is still work to be done to understand the long-term biological risks associated with low-dose radiation. In the study of long-term genomic effects of radiation, Monte Carlo simulations should be used to analyze radiation tracks, to investigate the origin of a patchwork pattern of large DNA deletions [5], or to investigate chromatin structural changes using Hi-C methods that cannot be detected from genome sequences. In the study of long-term metabolic effects of radiation, the influence of mitochondrial activation should be investigated by measuring ROS levels, and the detection of SASP factors and the investigation of which secretory factors are expressed at what levels is necessary to study the long-term effects on normal surrounding cells not directly exposed to radiation.

Finally, I would like to mention leukemia in survivors of the atomic bombings of Hiroshima and Nagasaki. Leukemia often occurred after a latency period of 6 to 7 years after exposure, and solid cancers increased in a dose-dependent manner over a latency period of 10 to 40 years after the leukemia peak. Despite the fact that more than 70 years have passed since the atomic bombings, it is known that the risk of solid cancers in atomic bomb survivors remains high [6]. Radiation research in the biological field should be applicable to accurately assess the long-term health effects of atomic bomb survivors or residents near the Fukushima Daiichi nuclear power plant who may be faced with anxiety of radiation exposure resulting from the accident. I believe that my work in this thesis brings us one step closer to elucidating the long-term genetic and metabolic effects of radiation.

REFERENCES

CHAPTER 1: Introduction

1. BEIR, V. Health Effects of Exposure to Low Levels of Ionizing Radiation. *Natl Academy Pr* **1990**.

2. Suzuki, K.; Ojima, M.; Kodama, S.; Watanabe, M. Radiation-induced DNA damage and delayed induced genomic instability. *Oncogene* **2003**, *22*, 6988-6993, doi:10.1038/sj.onc.1206881.

3. Kumari, R.; Jat, P. Mechanisms of Cellular Senescence: Cell Cycle Arrest and Senescence Associated Secretory Phenotype. *Front Cell Dev Biol* **2021**, *9*, 645593, doi:10.3389/fcell.2021.645593.

4. Ledingham, K.W.D.; Bolton, P.R.; Shikazono, N.; Ma, C.-M.C. Towards Laser Driven Hadron Cancer Radiotherapy: A Review of Progress. *Appl. Sci.* **2014**, *4*, 402-443, doi:org/10.3390/app4030402

5. Joiner, M; van der Kogel A. Basic Clinical Radiobiology. 4th ed. Edward Arnold. **2009**. The time-scale of effects in radiation biology.

6. Adams, G.E.; Jameson, D.G. Time effects in molecular radiation biology. *Radiat Environ Biophys* **1980**, *17*, 95-113, doi:10.1007/BF02027847.

7. O'Neill, P. Fielden, EM. Primary Free Radical Processes in DNA. *Adv Radiat Biol* **1993**, 17,53–120. doi:10.1016/B978-0-12-035417-7.50005-2

8. Kaina, B. DNA damage-triggered apoptosis: critical role of DNA repair, double-strand breaks, cell proliferation and signaling. *Biochem Pharmacol* **2003**, *66*, 1547-1554, doi:10.1016/s0006-2952(03)00510-0.

9. Suzuki, K.; Yokoyama, S.; Waseda, S.; Kodama, S.; Watanabe, M. Delayed reactivation of p53 in the progeny of cells surviving ionizing radiation. *Cancer Res* **2003**, *63*, 936-941.

10. Moon, J.J.; Lu, A.; Moon, C. Role of genomic instability in human carcinogenesis. *Exp Biol Med (Maywood)* **2019**, *244*, 227-240, doi:10.1177/1535370219826031.

11. Birch, J.; Gil, J. Senescence and the SASP: many therapeutic avenues. *Genes Dev* **2020**, *34*, 1565-1576, doi:10.1101/gad.343129.120.

12. Gorgojo, L.; Little, J.B. Expression of lethal mutations in progeny of irradiated mammalian cells. *Int J Radiat Biol* **1989**, *55*, 619-630, doi:10.1080/09553008914550661.

13. Seymour, C.B.; Mothersill, C.; Alper, T. High yields of lethal mutations in somatic mammalian cells that survive ionizing radiation. *Int J Radiat Biol Relat Stud Phys Chem Med* **1986**, *50*, 167-179, doi:10.1080/09553008614550541.

14. Marder, B.A.; Morgan, W.F. Delayed chromosomal instability induced by DNA damage. *Mol Cell Biol* **1993**, *13*, 6667-6677, doi:10.1128/mcb.13.11.6667-6677.1993.

15. Romney, C.A.; Paulauskis, J.D.; Nagasawa, H.; Little, J.B. Multiple manifestations of X-ray-induced genomic instability in Chinese hamster ovary (CHO) cells. *Mol Carcinog* **2001**, *32*, 118-127, doi:10.1002/mc.1071.

16. Suzuki, K.; Ojima, M.; Kodama, S.; Watanabe, M. Delayed activation of DNA damage checkpoint and radiation-induced genomic instability. *Mutat Res* **2006**, *597*, 73-77, doi:10.1016/j.mrfmmm.2005.04.024.

17. Brennan, R.J.; Schiestl, R.H. Persistent genomic instability in the yeast Saccharomyces cerevisiae induced by ionizing radiation and DNA-damaging agents. *Radiat Res* **2001**, *155*, 768-777, doi:10.1667/0033-7587(2001)155[0768:pgiity]2.0.co;2.

18. HAFF, R.F.; SWIM, H.E. Serial propagation of 3 strains of rabbit fibroblasts; their susceptibility to infection with vaccinia virus. *Proc Soc Exp Biol Med* **1956**, *93*, 200-204, doi:10.3181/00379727-93-22707.

19. HAYFLICK, L.; MOORHEAD, P.S. The serial cultivation of human diploid cell strains. *Exp Cell Res* **1961**, *25*, 585-621, doi:10.1016/0014-4827(61)90192-6.

20. Sahin, E.; Colla, S.; Liesa, M.; Moslehi, J.; Müller, F.L.; Guo, M.; Cooper, M.; Kotton, D.; Fabian, A.J.; Walkey, C.; et al. Telomere dysfunction induces metabolic and mitochondrial compromise. *Nature* **2011**, *470*, 359-365, doi:10.1038/nature09787.

21. Rodier, F.; Campisi, J. Four faces of cellular senescence. *J Cell Biol* **2011**, *192*, 547-556, doi:10.1083/jcb.201009094.

CHAPTER 2: Genomic effects

1. Morgan, W.F.; Day, J.P.; Kaplan, M.I.; McGhee, E.M.; Limoli, C.L. Genomic instability induced by ionizing radiation. *Radiat Res* **1996**, *146*, 247-258.

2. Seymour, C.B.; Mothersill, C.; Alper, T. High yields of lethal mutations in somatic mammalian cells that survive ionizing radiation. *Int J Radiat Biol Relat Stud Phys Chem Med* **1986**, *50*, 167-179, doi:10.1080/09553008614550541.

3. PUCK, T.T.; MARCUS, P.I. Action of x-rays on mammalian cells. *J Exp Med* **1956**, *103*, 653-666, doi:10.1084/jem.103.5.653.

4. Toyokuni, H.; Maruo, A.; Suzuki, K.; Watanabe, M. The contribution of radiation-induced large deletion of the genome to chromosomal instability. *Radiat Res* **2009**, *171*, 198-203, doi:10.1667/RR1464.1.

5. Suzuki, K.; Ojima, M.; Kodama, S.; Watanabe, M. Radiation-induced DNA damage and delayed induced genomic instability. *Oncogene* **2003**, *22*, 6988-6993, doi:10.1038/sj.onc.1206881.

6. Harper, K.; Lorimore, S.A.; Wright, E.G. Delayed appearance of radiation-induced mutations at the Hprt locus in murine hemopoietic cells. *Exp Hematol* **1997**, *25*, 263-269.

7. Suzuki, K.; Mitsutake, N.; Saenko, V.; Yamashita, S. Radiation signatures in childhood thyroid cancers after the Chernobyl accident: possible roles of radiation in carcinogenesis. *Cancer Sci* **2015**, *106*, 127-133, doi:10.1111/cas.12583.

8. Suzuki, K.; Ojima, M.; Kodama, S.; Watanabe, M. Delayed activation of DNA damage checkpoint and radiation-induced genomic instability. *Mutat Res* **2006**, *597*, 73-77, doi:10.1016/j.mrfmmm.2005.04.024.

9. Sarni, D.; Sasaki, T.; Irony Tur-Sinai, M.; Miron, K.; Rivera-Mulia, J.C.; Magnuson, B.; Ljungman, M.; Gilbert, D.M.; Kerem, B. 3D genome organization contributes to genome instability at fragile sites. *Nat Commun* **2020**, *11*, 3613, doi:10.1038/s41467-020-17448-2.

10. Valton, A.L.; Dekker, J. TAD disruption as oncogenic driver. *Curr Opin Genet Dev* **2016**, *36*, 34-40, doi:10.1016/j.gde.2016.03.008.

11. Flavahan, W.A.; Drier, Y.; Liau, B.B.; Gillespie, S.M.; Venteicher, A.S.; Stemmer-Rachamimov, A.O.; Suvà, M.L.; Bernstein, B.E. Insulator dysfunction and oncogene activation in IDH mutant gliomas. *Nature* **2016**, *529*, 110-114, doi:10.1038/nature16490.

12. Tubbs, A.; Nussenzweig, A. Endogenous DNA Damage as a Source of Genomic Instability in Cancer. *Cell* **2017**, *168*, 644-656, doi:10.1016/j.cell.2017.01.002.

13. Elledge, S.J. Cell cycle checkpoints: preventing an identity crisis. *Science* **1996**, *274*, 1664-1672, doi:10.1126/science.274.5293.1664.

14. Zhivotovsky, B.; Kroemer, G. Apoptosis and genomic instability. *Nat Rev Mol Cell Biol* **2004**, *5*, 752-762, doi:10.1038/nrm1443.Hanahan, D.; Weinberg, R.A. The hallmarks of cancer. *Cell* **2000**, *100*, 57-70, doi:10.1016/s0092-8674(00)81683-9.

15. Yao, Y.; Dai, W. Genomic Instability and Cancer. *J Carcinog Mutagen* **2014**, *5*, doi:10.4172/2157-2518.1000165.

16. Chetverina, D.; Fujioka, M.; Erokhin, M.; Georgiev, P.; Jaynes, J.B.; Schedl, P. Boundaries of loop domains (insulators): Determinants of chromosome form and function in multicellular eukaryotes. *Bioessays* **2017**, *39*, doi:10.1002/bies.201600233.

17. Blaisdell, J.O.; Wallace, S.S. Abortive base-excision repair of radiation-induced clustered DNA lesions in Escherichia coli. *Proc Natl Acad Sci U S A* **2001**, *98*, 7426-7430, doi:10.1073/pnas.131077798.

18. Prise, K.M.; Pullar, C.H.; Michael, B.D. A study of endonuclease III-sensitive sites in irradiated DNA: detection of alpha-particle-induced oxidative damage. *Carcinogenesis* **1999**, *20*, 905-909, doi:10.1093/carcin/20.5.905.

19. Sutherland, B.M.; Bennett, P.V.; Sidorkina, O.; Laval, J. Clustered damages and total lesions induced in DNA by ionizing radiation: oxidized bases and strand breaks. *Biochemistry* **2000**, *39*, 8026-8031, doi:10.1021/bi9927989.

20. Sutherland, B.M.; Bennett, P.V.; Sidorkina, O.; Laval, J. Clustered DNA damages induced in isolated DNA and in human cells by low doses of ionizing radiation. *Proc Natl Acad Sci U S A* **2000**, *97*, 103-108, doi:10.1073/pnas.97.1.103.

21. Hirose, E.; Suzuki, K.; Yokoya, A. Molecular Configuration of Human Genome Neighboring Megabase-Sized Large Deletions Induced by X-Ray Irradiation. *Radiat Res* **2021**, *195*, 561-567, doi:10.1667/RR15229.1.

22. Goodhead, D.T. Initial events in the cellular effects of ionizing radiations: clustered damage in DNA. *Int J Radiat Biol* **1994**, *65*, 7-17, doi:10.1080/09553009414550021.

23. Lemire, M.; Zaidi, S.H.; Ban, M.; Ge, B.; Aïssi, D.; Germain, M.; Kassam, I.; Wang, M.; Zanke, B.W.; Gagnon, F.; et al. Long-range epigenetic regulation is conferred by genetic variation located at thousands of independent loci. *Nat Commun* **2015**, *6*, 6326, doi:10.1038/ncomms7326.

24. Qiu, Z.; Zhang, Z.; Roschke, A.; Varga, T.; Aplan, P.D. Generation of Gross Chromosomal Rearrangements by a Single Engineered DNA Double Strand Break. *Sci Rep* **2017**, *7*, 43156, doi:10.1038/srep43156.

25. Ward, J.F. DNA damage produced by ionizing radiation in mammalian cells: identities, mechanisms of formation, and reparability. *Prog Nucleic Acid Res Mol Biol* **1988**, *35*, 95-125, doi:10.1016/s0079-6603(08)60611-x.

26. Liu, Y.; Nanni, L.; Sungalee, S.; Zufferey, M.; Tavernari, D.; Mina, M.; Ceri, S.; Oricchio, E.; Ciriello, G. Systematic inference and comparison of multi-scale chromatin sub-compartments connects spatial organization to cell phenotypes. *Nat Commun* **2021**, *12*, 2439, doi:10.1038/s41467-021-22666-3.

27. Sarni, D.; Sasaki, T.; Irony Tur-Sinai, M.; Miron, K.; Rivera-Mulia, J.C.; Magnuson, B.; Ljungman, M.; Gilbert, D.M.; Kerem, B. 3D genome organization contributes to genome instability at fragile sites. *Nat Commun* **2020**, *11*, 3613, doi:10.1038/s41467-020-17448-2.
28. Miura, H.; Takahashi, S.; Poonperm, R.; Tanigawa, A.; Takebayashi, S.I.; Hiratani, I. Single-cell DNA replication profiling identifies spatiotemporal developmental dynamics of chromosome organization. *Nat Genet* **2019**, *51*, 1356-1368, doi:10.1038/s41588-019-0474-z.
29. Akdemir, K.C.; Le, V.T.; Chandran, S.; Li, Y.; Verhaak, R.G.; Beroukhim, R.; Campbell, P.J.; Chin, L.; Dixon, J.R.; Futreal, P.A.; et al. Disruption of chromatin folding domains by somatic genomic rearrangements in human cancer. *Nat Genet* **2020**, *52*, 294-305, doi:10.1038/s41588-019-0564-y.
30. Watanabe, R.; Wada, S.; Funayama, T.; Kobayashi, Y.; Saito, K.; Furusawa, Y. Monte Carlo simulation of radial distribution of DNA strand breaks along the C and Ne ion paths. *Radiat Prot Dosimetry* **2011**, *143*, 186-190, doi:10.1093/rpd/ncq539.

CHAPTER 3: Metabolic effects

1. HAFF, R.F.; SWIM, H.E. Serial propagation of 3 strains of rabbit fibroblasts; their susceptibility to infection with vaccinia virus. *Proc Soc Exp Biol Med* **1956**, *93*, 200-204, doi:10.3181/00379727-93-22707.
2. HAYFLICK, L.; MOORHEAD, P.S. The serial cultivation of human diploid cell strains. *Exp Cell Res* **1961**, *25*, 585-621, doi:10.1016/0014-4827(61)90192-6.
3. Johmura, Y.; Shimada, M.; Misaki, T.; Naiki-Ito, A.; Miyoshi, H.; Motoyama, N.; Ohtani, N.; Hara, E.; Nakamura, M.; Morita, A.; et al. Necessary and sufficient role for a mitosis skip in senescence induction. *Mol Cell* **2014**, *55*, 73-84, doi:10.1016/j.molcel.2014.05.003.
4. Ewald, J.A.; Desotelle, J.A.; Wilding, G.; Jarrard, D.F. Therapy-induced senescence in cancer. *J Natl Cancer Inst* **2010**, *102*, 1536-1546, doi:10.1093/jnci/djq364.
5. Saleh, T.; Bloukh, S.; Carpenter, V.J.; Alwohoush, E.; Bakeer, J.; Darwish, S.; Azab, B.; Gewirtz, D.A. Therapy-Induced Senescence: An "Old" Friend Becomes the Enemy. *Cancers (Basel)* **2020**, *12*, doi:10.3390/cancers12040822.
6. Jones, K.R.; Elmore, L.W.; Jackson-Cook, C.; Demasters, G.; Povirk, L.F.; Holt, S.E.; Gewirtz, D.A. p53-Dependent accelerated senescence induced by ionizing radiation in breast tumour cells. *Int J Radiat Biol* **2005**, *81*, 445-458, doi:10.1080/09553000500168549.

7. Patel, N.H.; Sohal, S.S.; Manjili, M.H.; Harrell, J.C.; Gewirtz, D.A. The Roles of Autophagy and Senescence in the Tumor Cell Response to Radiation. *Radiat Res* **2020**, *194*, 103-115, doi:10.1667/RADE-20-00009.

8. Suzuki, M.; Yamauchi, M.; Oka, Y.; Suzuki, K.; Yamashita, S. Live-cell imaging visualizes frequent mitotic skipping during senescence-like growth arrest in mammary carcinoma cells exposed to ionizing radiation. *Int J Radiat Oncol Biol Phys* **2012**, *83*, e241-250, doi:10.1016/j.ijrobp.2011.12.003.

9. Mária, J.; Ingrid, Ž. Effects of bioactive compounds on senescence and components of senescence associated secretory phenotypes in vitro. *Food Funct* **2017**, *8*, 2394-2418, doi:10.1039/c7fo00161d.

10. Stein, G.H.; Drullinger, L.F.; Soulard, A.; Dulić, V. Differential roles for cyclin-dependent kinase inhibitors p21 and p16 in the mechanisms of senescence and differentiation in human fibroblasts. *Mol Cell Biol* **1999**, *19*, 2109-2117, doi:10.1128/MCB.19.3.2109.

11. McConnell, B.B.; Gregory, F.J.; Stott, F.J.; Hara, E.; Peters, G. Induced expression of p16(INK4a) inhibits both CDK4- and CDK2-associated kinase activity by reassortment of cyclin-CDK-inhibitor complexes. *Mol Cell Biol* **1999**, *19*, 1981-1989, doi:10.1128/MCB.19.3.1981.

12. Blagosklonny, M.V. Cell senescence, rapamycin and hyperfunction theory of aging. *Cell Cycle* **2022**, *21*, 1456-1467, doi:10.1080/15384101.2022.2054636.

13. Blagosklonny, M.V. Hallmarks of cancer and hallmarks of aging. *Aging (Albany NY)* **2022**, *14*, 4176-4187, doi:10.18632/aging.204082.

14. Kobashigawa, S.; Suzuki, K.; Yamashita, S. Ionizing radiation accelerates Drp1-dependent mitochondrial fission, which involves delayed mitochondrial reactive oxygen species production in normal human fibroblast-like cells. *Biochem Biophys Res Commun* **2011**, *414*, 795-800, doi:10.1016/j.bbrc.2011.10.006.

15. Agarwal, P.; Sandey, M.; DeInnocentes, P.; Bird, R.C. Tumor suppressor gene p16/INK4A/CDKN2A-dependent regulation into and out of the cell cycle in a spontaneous canine model of breast cancer. *J Cell Biochem* **2013**, *114*, 1355-1363, doi:10.1002/jcb.24476.

16. HARMAN, D. Aging: a theory based on free radical and radiation chemistry. *J Gerontol* **1956**, *11*, 298-300, doi:10.1093/geronj/11.3.298.

17. Wiley, C.D.; Velarde, M.C.; Lecot, P.; Liu, S.; Sarnoski, E.A.; Freund, A.; Shirakawa, K.; Lim, H.W.; Davis, S.S.; Ramanathan, A.; et al. Mitochondrial Dysfunction Induces Senescence with a Distinct Secretory Phenotype. *Cell Metab* **2016**, *23*, 303-314, doi:10.1016/j.cmet.2015.11.011.

18. Serrano, M.; Lin, A.W.; McCurrach, M.E.; Beach, D.; Lowe, S.W. Oncogenic ras provokes premature cell senescence associated with accumulation of p53 and p16INK4a. *Cell* **1997**, *88*, 593-602, doi:10.1016/s0092-8674(00)81902-9.

19. Bratic, I.; Trifunovic, A. Mitochondrial energy metabolism and ageing. *Biochim Biophys Acta* **2010**, *1797*, 961-967, doi:10.1016/j.bbabio.2010.01.004.

20. Young, A.R.; Narita, M.; Ferreira, M.; Kirschner, K.; Sadaie, M.; Darot, J.F.; Tavaré, S.; Arakawa, S.; Shimizu, S.; Watt, F.M. Autophagy mediates the mitotic senescence transition. *Genes Dev* **2009**, *23*, 798-803, doi:10.1101/gad.519709.

21. Skog, S.; Tribukait, B.; Sundius, G. Energy metabolism and ATP turnover time during the cell cycle of Ehrlich ascites tumour cells. *Exp Cell Res* **1982**, *141*, 23-29, doi:10.1016/0014-4827(82)90063-5.

22. Suzuki, K.; Mori, I.; Nakayama, Y.; Miyakoda, M.; Kodama, S.; Watanabe, M. Radiation-induced senescence-like growth arrest requires TP53 function but not telomere shortening. *Radiat Res* **2001**, *155*, 248-253, doi:10.1667/0033-7587(2001)155[0248:rislga]2.0.co;2.

23. Suzuki, M.; Boothman, D.A. Stress-induced premature senescence (SIPS)--influence of SIPS on radiotherapy. *J Radiat Res* **2008**, *49*, 105-112, doi:10.1269/jrr.07081.

24. Cai, Y.; Zhou, H.; Zhu, Y.; Sun, Q.; Ji, Y.; Xue, A.; Wang, Y.; Chen, W.; Yu, X.; Wang, L.; et al. Elimination of senescent cells by β-galactosidase-targeted prodrug attenuates inflammation and restores physical function in aged mice. *Cell Res* **2020**, *30*, 574-589, doi:10.1038/s41422-020-0314-9.

25. Zhao, H.; Zhuang, Y.; Li, R.; Liu, Y.; Mei, Z.; He, Z.; Zhou, F.; Zhou, Y. Effects of different doses of X-ray irradiation on cell apoptosis, cell cycle, DNA damage repair and glycolysis in HeLa cells. *Oncol Lett* **2019**, *17*, 42-54, doi:10.3892/ol.2018.9566.

26. Oka, Y.; Yamauchi, M.; Suzuki, M.; Yamashita, S.; Suzuki, K. Persistence and dynamics of DNA damage signal amplification determined by microcolony formation and live-cell imaging. *J Radiat Res* **2011**, *52*, 766-774, doi:10.1269/jrr.10164.

27. Dimri, G.P.; Lee, X.; Basile, G.; Acosta, M.; Scott, G.; Roskelley, C.; Medrano, E.E.; Linskens, M.; Rubelj, I.; Pereira-Smith, O. A biomarker that identifies senescent human cells in culture and in aging skin in vivo. *Proc Natl Acad Sci U S A* **1995**, *92*, 9363-9367, doi:10.1073/pnas.92.20.9363.

28. HAYFLICK, L. THE LIMITED IN VITRO LIFETIME OF HUMAN DIPLOID CELL STRAINS. *Exp Cell Res* **1965**, *37*, 614-636, doi:10.1016/0014-4827(65)90211-9.

29. Kam, W.W.; Banati, R.B. Effects of ionizing radiation on mitochondria. *Free Radic Biol Med* **2013**, *65*, 607-619, doi:10.1016/j.freeradbiomed.2013.07.024.

30. Kaminaga, K.; Hamada, R.; Usami, N.; Suzuki, K.; Yokoya, A. Targeted Nuclear Irradiation with an X-Ray Microbeam Enhances Total JC-1 Fluorescence from Mitochondria. *Radiat Res* **2020**, *194*, 511-518, doi:10.1667/RR15110.1.

31. Boengler, K.; Heusch, G.; Schulz, R. Nuclear-encoded mitochondrial proteins and their role in cardioprotection. *Biochim Biophys Acta* **2011**, *1813*, 1286-1294, doi:10.1016/j.bbamcr.2011.01.009.

32. Klingenberg, M. The ADP and ATP transport in mitochondria and its carrier. *Biochim Biophys Acta* **2008**, *1778*, 1978-2021, doi:10.1016/j.bbamem.2008.04.011.

33. Klingenberg, M.; Rottenberg, H. Relation between the gradient of the ATP/ADP ratio and the membrane potential across the mitochondrial membrane. *Eur J Biochem* **1977**, *73*, 125-130, doi:10.1111/j.1432-1033.1977.tb11298.x.

34. Yao, G.D.; Yang, J.; Li, X.X.; Song, X.Y.; Hayashi, T.; Tashiro, S.I.; Onodera, S.; Song, S.J.; Ikejima, T. Blocking the utilization of glucose induces the switch from senescence to apoptosis in pseudolaric acid B-treated human lung cancer cells in vitro. *Acta Pharmacol Sin* **2017**, *38*, 1401-1411, doi:10.1038/aps.2017.39.

35. Correia-Melo, C.; Marques, F.D.; Anderson, R.; Hewitt, G.; Hewitt, R.; Cole, J.; Carroll, B.M.; Miwa, S.; Birch, J.; Merz, A.; et al. Mitochondria are required for pro-ageing features of the senescent phenotype. *EMBO J* **2016**, *35*, 724-742, doi:10.15252/embj.201592862.

36. Sahin, E.; Colla, S.; Liesa, M.; Moslehi, J.; Müller, F.L.; Guo, M.; Cooper, M.; Kotton, D.; Fabian, A.J.; Walkey, C.; et al. Telomere dysfunction induces metabolic and mitochondrial compromise. *Nature* **2011**, *470*, 359-365, doi:10.1038/nature09787.

37. Westermann, B.; Bioenergetic role of mitochondrial fusion and fission. *Biochim Biophys Acta* **2012**, *1817*, 1833-1838, doi:10.1016/j.bbabio.2012.02.033.

38. Miranda, S.; Correia, M.; Dias, A.G.; Pestana, A.; Soares, P.; Nunes, J.; Lima, J.; Máximo, V.; Boaventura, P. Evaluation of the role of mitochondria in the non-targeted effects of ionizing radiation using cybrid cellular models. *Sci Rep* **2020**, *10*, 6131, doi:10.1038/s41598-020-63011-w.

CHAPTER 4: Conclusion and future perspectives

1. Hirose, E.; Suzuki, K.; Yokoya, A. Molecular Configuration of Human Genome Neighboring Megabase-Sized Large Deletions Induced by X-Ray Irradiation. *Radiat Res* **2021**, *195*, 561-567, doi:10.1667/RR15229.1.

2. Hirose, E.; Yokoya, A.; Kawamura, K.; Suzuki, K. Analysis of differentially expressed genes on human X chromosome harboring large deletion induced by X-rays. *J Radiat Res* **2023**, doi:10.1093/jrr/rrac093.

3. Hirose, E.; Noguchi, M.; Ihara, T.; Yokoya, A. Mitochondrial Metabolism in X-Irradiated Cells Undergoing Irreversible Cell-Cycle Arrest. *Int J Mol Sci* **2023**, *24*, doi:10.3390/ijms24031833.

4. Hattori, Y.; Yokoya, A.; Watanabe, R. Cellular automaton-based model for radiation-induced bystander effects. *BMC Syst Biol* **2015**, *9*, 90, doi:10.1186/s12918-015-0235-2.

5. Watanabe, R.; Wada, S.; Funayama, T.; Kobayashi, Y.; Saito, K.; Furusawa, Y. Monte Carlo simulation of radial distribution of DNA strand breaks along the C and Ne ion paths. *Radiat Prot Dosimetry* **2011**, *143*, 186-190, doi:10.1093/rpd/ncq539.

6. Preston, D.L.; Pierce, D.A.; Shimizu, Y.; Cullings, H.M.; Fujita, S.; Funamoto, S.; Kodama, K. Effect of recent changes in atomic bomb survivor dosimetry on cancer mortality risk estimates. *Radiat Res* **2004**, *162*,]377-389, doi:10.1667/rr3232.